



HAL
open science

Multi-scale study of the transitional shock-wave boundary layer interaction in hypersonic flow

Mathieu Lugrin, Samir Beneddine, Eric Garnier, Reynald Bur

► To cite this version:

Mathieu Lugrin, Samir Beneddine, Eric Garnier, Reynald Bur. Multi-scale study of the transitional shock-wave boundary layer interaction in hypersonic flow. *Theoretical and Computational Fluid Dynamics*, In press, 10.1007/s00162-021-00595-7 . hal-03487084

HAL Id: hal-03487084

<https://hal.science/hal-03487084v1>

Submitted on 17 Dec 2021

HAL is a multi-disciplinary open access archive for the deposit and dissemination of scientific research documents, whether they are published or not. The documents may come from teaching and research institutions in France or abroad, or from public or private research centers.

L'archive ouverte pluridisciplinaire **HAL**, est destinée au dépôt et à la diffusion de documents scientifiques de niveau recherche, publiés ou non, émanant des établissements d'enseignement et de recherche français ou étrangers, des laboratoires publics ou privés.

Multi-scale study of the transitional shock-wave boundary layer interaction in hypersonic flow

Mathieu Lugin · Samir Beneddine · Eric Garnier · Reynald Bur

Received: date / Accepted: date

Abstract A high-fidelity simulation of the massively separated shock/ transitional boundary layer interaction caused by a 15-degrees axisymmetrical compression ramp is performed at a free stream Mach number of 6 and a transitional Reynolds number. The chosen configuration yields a strongly multiscale dynamics of the flow as the separated region oscillates at low-frequency, and high-frequency transitional instabilities are triggered by the injection of a generic noise at the inlet of the simulation. The simulation is post-processed using Proper Orthogonal Decomposition to extract the large scale low-frequency dynamics of the recirculation region. The bubble dynamics from the simulation is then compared to the results of a global linear stability analysis about the mean flow. A critical interpretation of the eigenspectrum of the linearized Navier-Stokes operator is presented. The recirculation region dynamics is found to be dominated by two coexisting modes, a quasi-steady one that expresses itself mainly in the reattachment region and that is caused by the interaction of two self-sustained instabilities, and an unsteady one linked with the separation shock-wave and the mixing layer. The unsteady mode is driven by a feedback loop in the recirculation region, which may also be relevant for other unsteady shock-motion already documented for shock-wave/turbulent boundary layer interaction. The impact of the large-scale dynamics on the transitional one is then assessed through the numerical filtering of those low wavenumber modes; they are found to have no impact on the transitional dynamics.

Keywords Shock-wave/boundary layer interaction · Transition · Linear stability · High fidelity simulation

1 Introduction

One of the main challenges facing designer of hypersonic vehicles is the correct prediction of aerodynamic thermo-mechanical loads. If overestimated, they will lead to a severe increase in gross take-off weight. If underestimated, they may cause catastrophic failure of the vehicle. However, the mechanisms causing those loads are often complex and challenging to model. The present study focuses on transition through Shockwave-Boundary Layer Interaction (SBLI), a strongly multiscale and commonly encountered problem of the hypersonic flight.

First, transition to turbulence in hypersonic regimes commonly appears through the linear development and non-linear breakdown of small-scale instabilities at relatively high frequencies, which causes a severe heat-flux rise (transitional fluxes being higher than turbulent ones). This is especially important since in-flight conditions are often transitional. The rich state-of-the-art on the subject [1–6] illustrates how complex it is to know *a priori* which mechanism will lead to transition in hypersonic conditions, even for the simple cases of an attached boundary layer on a flat plate.

Then, the shock-wave boundary layer interaction makes the flow topology even more sensitive to transitional mechanisms, since laminar interactions lead to larger separated regions than turbulent one. Lugin *et al.* [6] confirmed that the mechanism found by Marxen et Rist [7] for incompressible separation bubbles is also relevant for hypersonic SBLI: transitional instabilities (and the associated receptivity mechanisms) play a central role in the definition of the recirculation region topology. Indeed, they found that the separated region size varies by several orders of magnitude depending on the ambient noise in their numerical simulations. Additionally, the separated region brings new instabilities leading to

transition, such as mixing layer modes [8], Görtler vortices [9] or the so-called reattachment vortices [10]. More importantly, multiple studies point to the existence of low-frequency large-scale dynamics in the laminar recirculation region. First, Robinet [11] found a global instability in a laminar supersonic SBLI flow, then Hildebrand *et al.* [12] and Sidhart *et al.* [13] showed that global instabilities of the bubble are also present in hypersonic SBLI and can lead to the apparition of streaks. Cao *et al.* [14] went even further and postulated that this global instability could cause the transition to turbulence without free-stream perturbations.

Another well-known feature of SBLI is the "breathing" motion of the separated region, which may lead to unsteady thermal and mechanical loads. The subject has been widely studied for shock-turbulent boundary layer interaction, either numerically [15–19] or experimentally [20]. For incipient separations, these interactions tend to be dominated by unsteadiness caused by the excitation through upstream turbulence [21]. However, the breathing of the bubble in turbulent flows may also be linked to a downstream scenario driven by an unstable mode of the bubble [22,23]. This is especially true for strongly separated flows [24].

The interest for transitional interaction, where the turbulent upstream scenario is irrelevant and both the laminar global mode and turbulent "downstream scenario" are unsure, only seems to be growing recently; for example, with the numerical study of Hildebrand *et al.* [12]. Results on transitional SBLI are still relatively rare, and the interactions of the bubble breathing and the globally unstable modes with the transitional instabilities have never been documented. While some studies cited here-before bring interesting information about the new instabilities and amplification mechanisms originating from the SBLI and the separated region, they mainly focus on one single type of instability or amplification mechanism and postulate that it may be responsible for transition to turbulence. Though, Bur *et al.* [25] experimentally studied the impact of transition through a SBLI on the European Pre-X demonstrator and showed that it is crucial to understand the transition process better when dealing with control surface separation in real-life designs. In this context, a study combining the multiple known mechanisms up to the actual transition is still lacking from the literature. It may help to distinguish the instabilities and amplification mechanisms that play an important role from those that are present but not directly involved in the transition process.

The present paper aims at providing new insights on this question by studying a transitional hypersonic flow on the geometry used by Benay *et al.* [26]. The model is a hollow cylinder followed by a 15° flare, and as explained in section 2.1, the flow conditions are set such that there is a large separated region. The goals of the study are the following. First, a full description of the low-frequency low-wavenumber dynamics of the separated region is still missing for this configuration and will be presented in this paper alongside an in-depth study of their underlying physical mechanisms. To do so, results from a Quasi Direct Numerical Simulation (QDNS), which is a highly resolved Wall Resolved Large Eddy Simulations (WRLES) with no subgrid scale modelling, are exploited. As discussed in [6], this type of simulation allows for reasonable computing time alongside a sufficient precision in the regions of interest (in this case, the laminar and transitional regions). The domain used for this simulation spans over 360° , allowing for large-scale modes to grow without constraints. Large-scale coherent structures are extracted from the simulations through Proper Orthogonal Decomposition (POD). The QDNS analysis is then coupled with a linear stability analysis about the mean flow to get insights into the underlying physical mechanisms. This leads to the second point of the study: the use of the mean-flow stability results to characterize the spatio-temporal behavior of the large-scale structures, which could not be fully addressed by the QDNS alone due to the (too) small timescale involved.

After characterizing the dynamics of the bubble, the final question of this article comes naturally: what are the interactions between the large-scale dynamics and the transitional one? It is essential to know how far one can go in reducing the azimuthal domain size before affecting the flow topology and transition process. This is also linked with the question of which mechanisms (*i.e.* convective mechanism [10] or absolutely unstable mechanisms [14,13]) creating streaks play an important role in the transition process in this case, where free-stream perturbations are present. To address this last point, two more QDNSs are conducted, covering reduced spans of the domain to select the wavenumbers of the modes that will be able to grow in each simulation. This allows to filter out the dominant bubble mode from the simulations, and thus to study their impact on both the topology of the flow and the transition process.

The article is organized as follows. First, the setup is presented, including the solver and computation parameters, the post-processing tools, and the linear stability framework. Then, the low-frequency dynamics of the recirculation bubble is characterized through the study of POD modes from the QDNS. For each mode, the underlying physical mechanisms are investigated through the study of the linearized Navier Stokes operator. The impact of the bubble dynamics on the transitional process is then assessed before concluding on the overall impact of the bubble modes on the flow.

Table 1 Free stream conditions and characteristic values for the simulation.

M_∞	T_∞	P_∞	U_∞	T_i
6	86.6 K	1023 Pa	1119 m/s	710 K
T_{wall}	Re_L	δ_{sep}	L_{sep}	L
290 K	1.95×10^6	0.00165 m	0.192 m	0.252 m

2 Numerical Setup

2.1 Flow configuration

The present paper is based on the geometry used in the experimental campaign of Benay *et al.* [26], the geometry is a hollow cylinder of diameter $D = 131\text{mm}$ and length $L = 252\text{mm}$ followed by a 15° flare, the total length of the geometry is 350mm . The geometry is presented in figure 1 alongside some information on the numerical domain and a numerical Schlieren visualization of the mean (time and azimuthal-averaged) flow. The flow conditions are not chosen from the existing experimental database (which brings no information on the dynamics of interest here). Instead, they are selected to maximize the importance of the separation. The Mach number is set to 6, and the free-stream conditions are chosen to obtain a transitional Reynolds number value. The free-stream is perturbed by a random white noise (see appendix 1) to trigger convective instabilities through their receptivity process. The perturbation level is chosen such that the boundary layer is laminar when interacting with the separation shock, causing a stronger separation. However, the flow is fully turbulent before the end of the domain, which encompasses the totality of the transition process. The free-stream conditions are presented in table 1 alongside the length of the separation region (L_{sep}) and the boundary layer thickness at the separation point (δ_{sep}).

2.2 Simulations

Three different numerical simulations of the unsteady flow are conducted using the high-performance finite volume multi-block structured "FAST" (Flexible Aerodynamic Solver Technology) solver from ONERA [27]. Viscous fluxes are computed using a second-order centered scheme. Convective fluxes are computed using the second-order upwind Advection Upstream Splitting Method AUSM(P) scheme proposed by Mary et Sagaut [28] with an unlimited third-order Monotonic Upstream-centered Scheme for Conservation Laws (MUSCL) reconstruction. The time integration is performed via an explicit third order 3-step Runge-Kutta scheme. The timestep is set to 10^{-8}s to ensure a Friedrichs-Lewy (CFL) number lower than 0.5 in the whole domain. For every simulation, the wall temperature is imposed at 290K, and standard supersonic inflow, outflow, and farfield conditions are used for the other boundaries. These are characteristics-based boundary conditions that avoid numerical reflections.

The three simulations are the following: one unfiltered 360° computation, and two spatially filtered simulations where only certain azimuthal wavenumbers m are retained. By confronting the unfiltered dynamics to those spatially filtered, we aim at assessing the impact of the small wavenumber dynamics (*i.e.* the large-scale bubble dynamics) on the larger wavenumber structures (smaller scale). The filtering is performed by restricting the azimuthal extent of the computational domain and imposing periodicity conditions on the azimuthal boundaries. The azimuthal extent and number of points in each mesh of the different simulations are presented in table 2. Contrary to the full (360°) domain, where every integer wavenumber up to the wavenumber associated to the smallest cell size is resolved, the QDNSs labeled B and C in table 2 are such that only m values multiple of 6 and 24 can develop, respectively. This restriction results from the reduced size of the domain and the imposed periodic boundary conditions: only an integer number of wavelengths can exist in the spanwise direction (otherwise, the periodicity conditions would lead to discontinuities in the flow fields). For instance, for the domain used in QDNS C, the span of 15° (1/24th of the full domain) only allows the development of structures with a wavenumber equal to 0, 24, 48, 72, 96, etc.

The present work aims at accurately simulating the low-frequency dynamics and transition to turbulence through the SBLI. Therefore, the accurate simulation of turbulent dynamics past the reattachment point is not of interest here. Lugin *et al.* [6] showed that in this context, it is unnecessary to satisfy fully resolved Direct Numerical Simulation (DNS) requirements and that QDNS requirements such as defined by Spalart [29] in the turbulent region are sufficient to study the transition dynamics accurately. As such, the meshes used for this study correspond to slightly refined versions of that used by Lugin *et al.* [6] (who provide a mesh convergence study for a different Mach number but at a similar Reynolds number). They are designed such that all the eddies upstream from the reattachment point and the large-scale structures downstream are fully resolved. Since the flow is hypersonic and the boundary layer at the reattachment

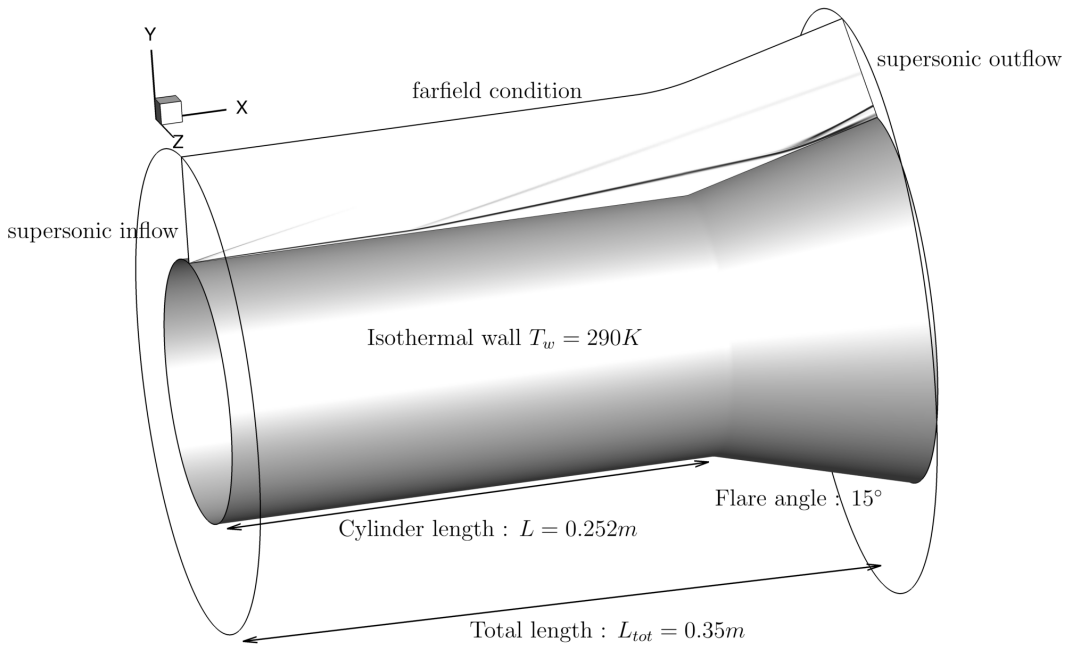


Fig. 1 Computational domain used in the full domain simulation showing boundary conditions and characteristics length. A numerical Schlieren of the mean flow is also shown.

Table 2 Mesh characteristics.

(Q)DNS	θ	n_x	n_r	n_θ	n_{tot}
A	360	1600	220	3600	1267M
B	60	1600	220	600	211M
C	15	1600	220	150	52.8M

point is compressed in a way that leads to a minimal subsonic region, there is virtually no feedback possible from the under-resolved turbulent region to the (well-resolved) upstream studied zone. In the under-resolved zone, the turbulent cascade is offset by the numerical viscosity of the upwind scheme [29] as the smallest scale structures are not properly resolved. However, these structures are only those near the end of the cascade (*i.e.* of very short wavelength, close to the Kolmogorov scale), and all the larger size eddies are still correctly resolved [29] (the spacing of the grid in the region of the mesh with the worst resolution is of the order $\Delta x^+ = 50$, $\Delta y^+ = 1$, $r\Delta\theta^+ = 25$). This means that while the turbulent statistics may be inaccurate in this zone, the topology and larger scale structures (compared to the Kolmogorov scale) are still accurately computed. It explains why Lugrin *et al.* [6] observed that their DNS and QDNS give similar results, even past the reattachment point. The QDNS allows for a reduction of one order of magnitude of the computational cost compared to a fully resolved DNS, bringing down the cost of this study from roughly 50 million to 5 million Central Processing Unit (CPU) hours.

Finally, as pointed out in the introduction, the flow is excited by an inlet noise following the procedure described in appendix 1. Inlet disturbances are needed to trigger the growth of transitional instabilities that are not self-sustained otherwise. In the wake of several recent articles that focused on transition to turbulence on similar configurations, the injected perturbations is a white noise that excites several mechanisms in the simulation, without targeting one in particular [5,6]. In the present study, the noise is injected into the inlet density. The inlet disturbances spectral content is flat (see figure 2). As stated before, the noise amplitude is chosen such that it leads to massive separation, leading to an amplitude of 1% of the local density. The numerical Schlieren visualization presented in figure 1 illustrates the massive separation.

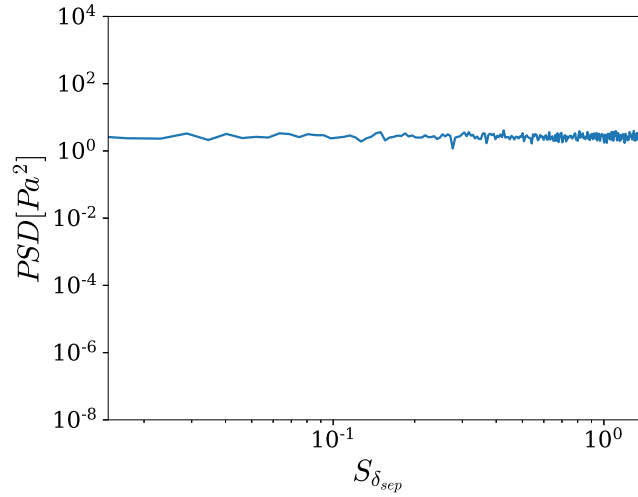


Fig. 2 Power spectral density of the wall pressure fluctuations showing the spectral content of the noise 3 cells downstream of the injection plane.

Table 3 Post-processing mesh characteristics.

QDNS	θ	n_x	n_r	n_θ	n_{tot}	$\Delta t_{sampling}$
Extraction	360	800	220	900	79.2M	$150\Delta_t$
Time filtered	360	400	110	900	39.6M	$150\Delta_t$
Time + azimuthal filtered	360	400	110	100	4.4M	$150\Delta_t$

2.3 Post-processing

Given the multiscale nature of the flow dynamics, different post-processing techniques may be used to accurately describe both the transitional and bubble dynamics. On the one hand, Spectral Proper Orthogonal Decomposition (SPOD), such as initially proposed by Lumley [30], has proven to be a powerful tool for the analysis of both turbulent [31,32] and transitional [6] high-fidelity simulations. It allows for the optimal extraction of spatiotemporally correlated modes from the simulation results. This technique has already been used successfully to study the transitional instabilities in a similar case [6]. However, computing SPOD modes for the low-frequency dynamics is out-of-reach in the present case since the required number of snapshots necessary to correctly converge the modes would be too high. As shown later, the large-scale dynamics is associated with frequencies as low as 100Hz or even lower. This may require simulating at the very least a physical duration of 0.1s (10 periods of the large-scale dynamics) to correctly compute SPOD modes at this frequency (i.e., 10 000 000 time steps). This would increase by one order of magnitude the cost of the present simulation and the amount of data to store and process, which are already the main limiting factors.

Therefore, a different strategy is proposed to extract the low-frequency modes based on successive decimation/filtering, which avoids aliasing while yielding a workable amount of data. The data processing is summed up in Fig. 3 and consists of the following steps. First, to get a manageable data amount to process, volumic snapshots from the QDNS are sampled every 150 time-step ($S_{L_{sep}} = fL_{sep}/U_\infty = 114, S_{\delta_{sep}} = f\delta_{sep}/U_\infty = 1, f = 666kHz$). They are also decimated in space: every other point in both the streamwise and wall-normal direction and every 4 points azimuthally. This down-sampling is limited enough to avoid aliasing both in time and space. Following this processing, 4000 snapshots are sampled from the full-domain DNS, representing 6ms of sampled signal and around 40 TB of raw data. Then, to isolate the low-frequency dynamics of the recirculation region, transitional and turbulent instabilities are filtered. Three different temporal Finite Impulse Response (FIR) filters have been designed with the Remez algorithm [33]. The frequency response of the filters are presented in figure 4. Every filter is of order 50, has a transition region of $S_{L_{sep}} = 4.3$ ($f = 25kHz$), and has a cutoff Strouhal number of $S_{L_{sep}}^{(c)} = f^{(c)}L_{sep}/U_\infty = 6.86$ ($f^{(c)} = 40kHz$), 1.72 ($f^{(c)} = 10kHz$) and 0.86 ($f^{(c)} = 5kHz$) respectively, with $f^{(c)}$ the cutoff frequency. All of those filters have a cutoff frequency that is relatively low compared to the frequency of transitional instabilities and turbulence. After applying the filter, the spatial resolution in the streamwise direction is divided by two to reduce the memory cost of the following treatment. Since this second decimation is performed after

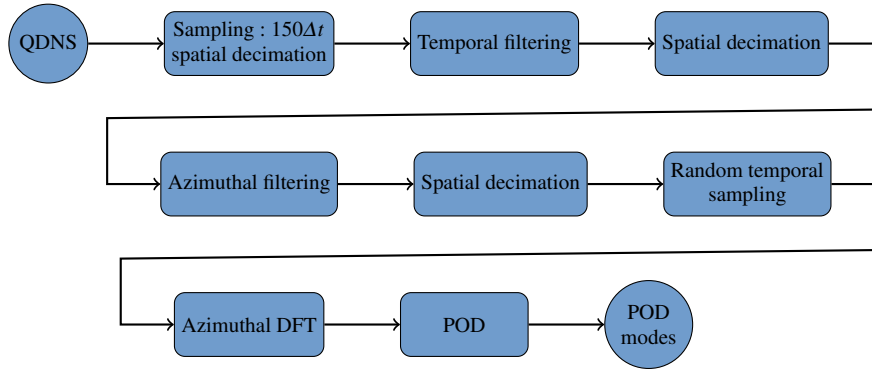


Fig. 3 Schematic of the treatment applied to data extracted from the QDNS.

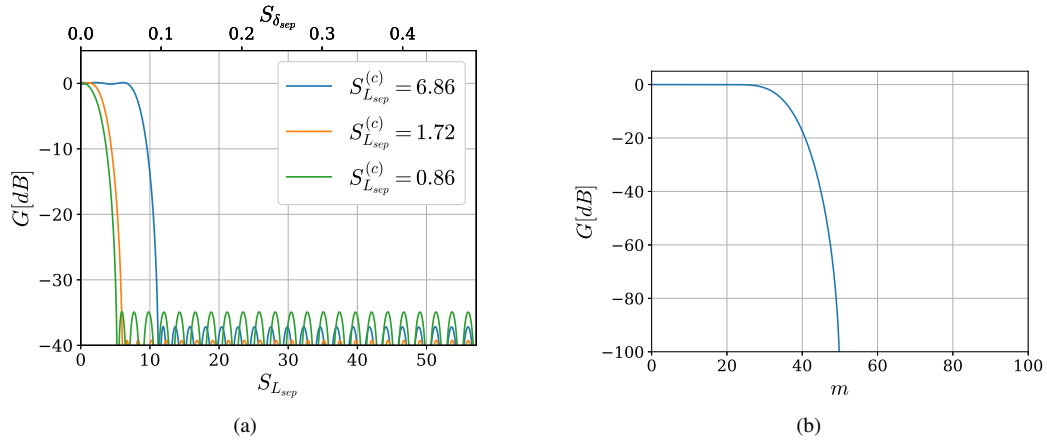


Fig. 4 (a): Transfer function of the three temporal low pass filters. (b): Transfer function of the azimuthal low pass filter.

the temporal filtering, it does not cause aliasing because all the small streamwise wavelength instabilities are oscillating at high frequency (and have already been filtered out by the temporal filter). Finally, given the difference in wavelength between the turbulent and transitional instabilities and the large-scale motion of the bubble, an azimuthal low pass filter of order 200, with a cutoff wavenumber of $m = 20$ and a transition region of 30, is applied (figure 4b, note that this filtering could have been done using a DFT instead of a FIR, which would have provided a perfect cutoff), followed by a last decimation in the azimuthal direction. This yields a total of 100 points in this direction to represent the whole domain. Recapitulating data of the meshes used for the post-processing are presented in table 3.

This procedure provides the snapshots used in the last step to extract large-scale coherent structures through an azimuthal decomposition, followed by a Proper Orthogonal Decomposition (POD). The numerical process to compute the POD modes is described in appendix 3. This yields spatial modes for each wavenumber of the form $\hat{\Psi}_i^{(m)} e^{jm\theta}$, where i is the mode rank (see appendix 3), j the complex constant and m the azimuthal wavenumber. This formulation is convenient as it allows to directly compare the two-dimensional (x, r) spatial form Ψ of the mode even for different wavenumbers. As the flow is statistically homogeneous in the azimuthal direction, the positive and negative azimuthal wavenumber modes mirror each other ($\hat{\Psi}_i^{(m)} = \hat{\Psi}_i^{(-m)}$). As explained in this appendix, it is possible to localize the decomposition to extract energetic coherent structures associated with a given region of the flow. In the following, when modes are presented, it will be either extracted from the whole domain or from the region upstream from the reattachment alone. In both cases, the region restriction will be systematically specified when presenting a mode. These two different localizations of the POD allow distinguishing between structures specific to the bubble dynamics and others.

2.4 Linear stability analysis

As previously shown by Marxen et Rist [7] and Lugin *et al.* [6], the study of the linearized Navier-Stokes operator about the mean flow is a powerful way to gain physical insights on instabilities of the separated region of the flow.

Despite the linear nature of the stability analysis, considering the mean flow instead of a steady solution (base flow) is a way to account for some non-linear effects (see McKeon et Sharma [34] and Beneddine *et al.* [35] for instance). In the case of a periodic dynamics characterized by a peaked temporal spectrum, the instabilities developing in the flow are linked to marginally stable/unstable eigenmodes $\hat{\mathbf{q}}$ of the linearized Navier-Stokes operator about the mean flow \mathbf{J} , at the frequency of the flow oscillation [36,37,35]. In the more general case where the unsteadiness is broadband, stability modes that describe the oscillations should still exist at a frequency ω loosely matching the dominant frequency. However, their growth rate σ may significantly depart from zero [37]. Therefore, in such a case, one may focus on the least stable/unstable modes in search of relevant modes, as it is likely that the dynamics is not described by marginally stable modes anymore.

However, the sign of the growth rate for those modes is not as easily interpretable as it would be for baseflow-based approaches. Contrary to a stability analysis about a steady solution of the Navier-Stokes equations, the modes about the mean flow (which is not a solution of the governing equations) do not represent the linear stage of the growth of disturbances. Therefore, its sign (*i.e.* the stable/unstable nature of the mode) is not physically relevant. This should be kept in mind when considering a mean flow stability analysis. Thus, this analysis will mainly bring information about the frequency and the spatial shape of some eigenmodes of interest. Note that even in a base flow stability analysis, the growth rate is not an indicator of which mode would be the most energetic within the flow (which is determined by non-linear saturation effects). For instance, the work of [38] is an example where the most energetic disturbances are not associated with the most unstable mode.

Additionally, the recent work from Karban *et al.* [39] revealed that the set of variables chosen to describe the dynamical system (*e.g.* primitive versus conservative) moderately affect the eigenspectrum values of the jacobian matrix. This further emphasizes the need not to over-interpret the growth rate values. On the contrary, the spatial structure of the modes (given by the eigenvectors) are almost unaffected by such variable choices. Therefore, they can be analyzed and compared with QDNS results more confidently.

To reduce the computing power needed for the linear stability analysis, one can take advantage of the azimuthal homogeneity of the mean flow to conduct independent studies for each wavenumber of interest. The implementation of the azimuthal decomposition presented hereafter comes initially from an idea of Schmid *et al.* [40] and was already used, for instance, by Paladini *et al.* and Lugin *et al.* [41,6]. It allows to perform the decomposition without having to derive azimuthally decomposed equations explicitly. The method is described in appendix 2. This approach is also convenient here since it makes the stability analysis directly comparable with the POD treatment described in 2.3: in both cases, modes are computed for each wavenumber m . The computed modes (which are eigenvectors of the operator) are then discrete 2D complex fields $\hat{\mathbf{q}}^{(m)}$. By definition, they are defined up to a complex multiplicative constant, and their real (and imaginary) part corresponds to an arbitrary slice of the 3D mode in the azimuthal direction. The complete (three-dimensional and time-dependent) dynamics of the mode is harmonic and given by the real part of $\hat{\mathbf{q}}^{(m)} e^{jm\theta + j\omega t}$, with ω the pulsation of the mode (the imaginary part of the eigenvalue associated with the mode). In the following, the modes will be presented as contours of the real part of $\hat{\mathbf{q}}^{(m)}$ which is equivalent to looking at the mode for a given angle and time.

To get more physical insights on the modes, the spatial region at the origin of the instability (the so-called "wave-maker") can be studied. This is usually done through the structural sensitivity approach developed by Giannetti et Luchini [42]. It involves the computation of adjoint modes (modes of the adjoint linearized operator): the structural sensitivity is computed as the local product of the norms of the direct and adjoint modes (see [42], [43] or [44] for further details). It yields a scalar field that quantifies how an eigenvalue is affected by introducing a localized feedback [41]. Therefore, it is helpful to identify the spatial zones responsible for the instability mechanism of a mode.

3 Large scale dynamics

3.1 Extraction of the dominant bubble modes from the QDNS data

This section is dedicated to the study of the shock-bubble system dynamics. As stated before, this dynamic is supposed to be of large spatial scale and low frequency (most studies pointing towards the existence of quasi-steady modes [12, 13, 11]). Thus, it is studied by processing filtered snapshots of the flow, such as described in section 2.3. This section aims to characterize the dominant modes.

The first interesting result is that the dominant POD modes (and their energetic content λ_0) computed from data filtered with the three different filters presented in section 2.3 are very similar. Fig 5 presents the differences between the leading POD modes when using filtered data with two different cutoff frequencies: $S_{Lsep}^{(c)} = 6.86$ versus $S_{Lsep}^{(c)} = 0.86$. First,

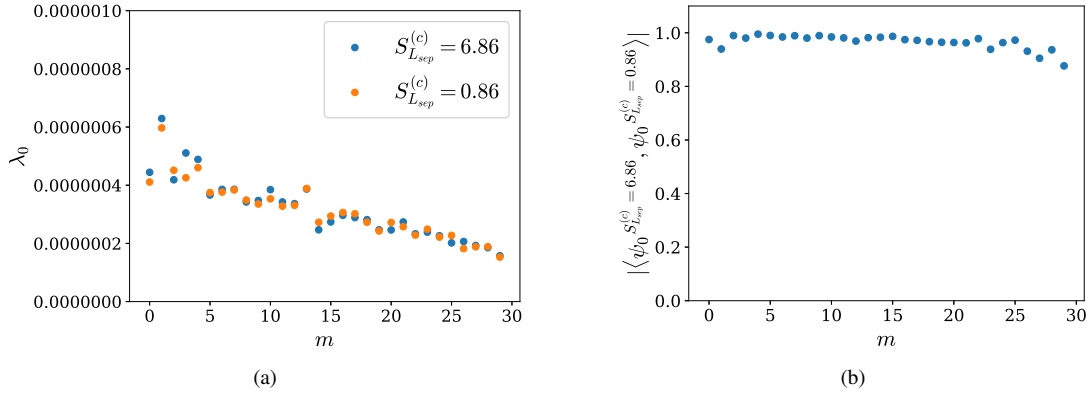


Fig. 5 Difference between the leading POD modes extracted from data filtered at $S_{Lsep}^{(c)} = 0.86$ and $S_{Lsep}^{(c)} = 6.86$: (a) present the relative change in energetic content, (b) the alignment coefficient between the two modes.

figure 5 (a) shows that the energetic content of the leading POD for each studied wavenumber is only slightly affected by the change of cutoff frequency. Additionally, the spatial organization of the modes is nearly not affected. One may quantify this last statement by computing an alignment coefficient [45], which is defined for two modes Ψ_a and Ψ_b as the normalized scalar product:

$$\frac{|\langle \Psi_a, \Psi_b \rangle|}{\sqrt{\langle \Psi_a, \Psi_a \rangle \langle \Psi_b, \Psi_b \rangle}}. \quad (1)$$

This coefficient is equal to 1 for perfectly aligned modes and 0 if they are orthogonal. Figure 5 (b) shows that the alignment coefficient between two corresponding modes with different cutoff frequencies is close to one for all the wavenumbers of interest. Therefore, the POD modes are virtually unaffected by the change in temporal filters. Besides proving that the bubble dynamics is, as expected, dominated by very low-frequency modes (*i.e.* at or below $S_{Lsep} = 0.86$), it shows that the study of the shock-bubble system dynamics may safely be conducted using the ($S_{Lsep}^{(c)} = 0.86$)-filtered data only. Indeed, no new modes nor important changes in the energetic content appear with the increase of $S_{Lsep}^{(c)}$ from 0.86 to 1.72 or 6.86.

Figure 6 (a) presents the energy in the leading POD modes for a wide range of wavenumbers extracted from the entire domain. It shows that a mode at $m = 1$ dominates the flow, and other modes display decreasing yet significant amounts of energy for higher wavenumbers. As known from previous numerical results [13, 12, 14], some bubble modes are linked to strong fluctuations in the reattachment region. To assess whether the modes relate to such reattachment dynamics, one may analyze how the POD modes are affected when the POD is bounded to the region upstream from the reattachment point ($x/L < 1.11$, see appendix 5 for details about the spatial bounding of the POD). Figure 6 (b) presents the energy of the leading POD modes for each wavenumber when such a spatial restriction is applied. When compared to figure 6 (a), one can notice that only the energetic content of the ($m = 1$)-mode remains nearly unchanged by this spatial restriction. This observation hints that the dominant ($m = 1$)-mode is mainly localized before reattachment in the separated region, which can be confirmed by computing the alignment coefficients of the leading modes computed with and without spatial restriction. This coefficient is close to one (0.970), confirming that the dominant ($m = 1$)-mode from the full domain is the same as the dominant one for the domain upstream of reattachment. The dynamics of this mode being mainly present in the separated region, it will be called mode B (bubble).

For higher wavenumbers ($m > 1$), the energy level of the dominant modes drastically decreases when switching from the spatially unbounded POD to the spatially bounded one, showing that their dynamics differs from mode B. Their energy content is mainly localized in the reattachment region, explaining the drop of energy when only considering the region $x/L < 1.11$. Moreover, apart from their azimuthal periodicity, all these ($m > 1$)-modes are extremely similar. This statement may be assessed by computing alignment coefficient between $\Psi_0^{(m)}$ and $\Psi_0^{(m')}$ for different wavenumbers $m > 1$ and $m' > 1$. An alignment coefficient matrix is presented in figure 8. The close-to-one value in the whole matrix confirms that all the modes have a very similar spatial organization in the (x, r) domain; they are all linked with the same physics. Therefore, these modes belong to a common group called modes R (reattachment) in the following.

On a side note, one has to be careful when interpreting the results at wavenumbers higher than 22 since the azimuthal filter starts to affect their energetic content significantly (see the characteristics of the azimuthal filter presented in figure 4 (b)). This is true for all the figures presented in this section.

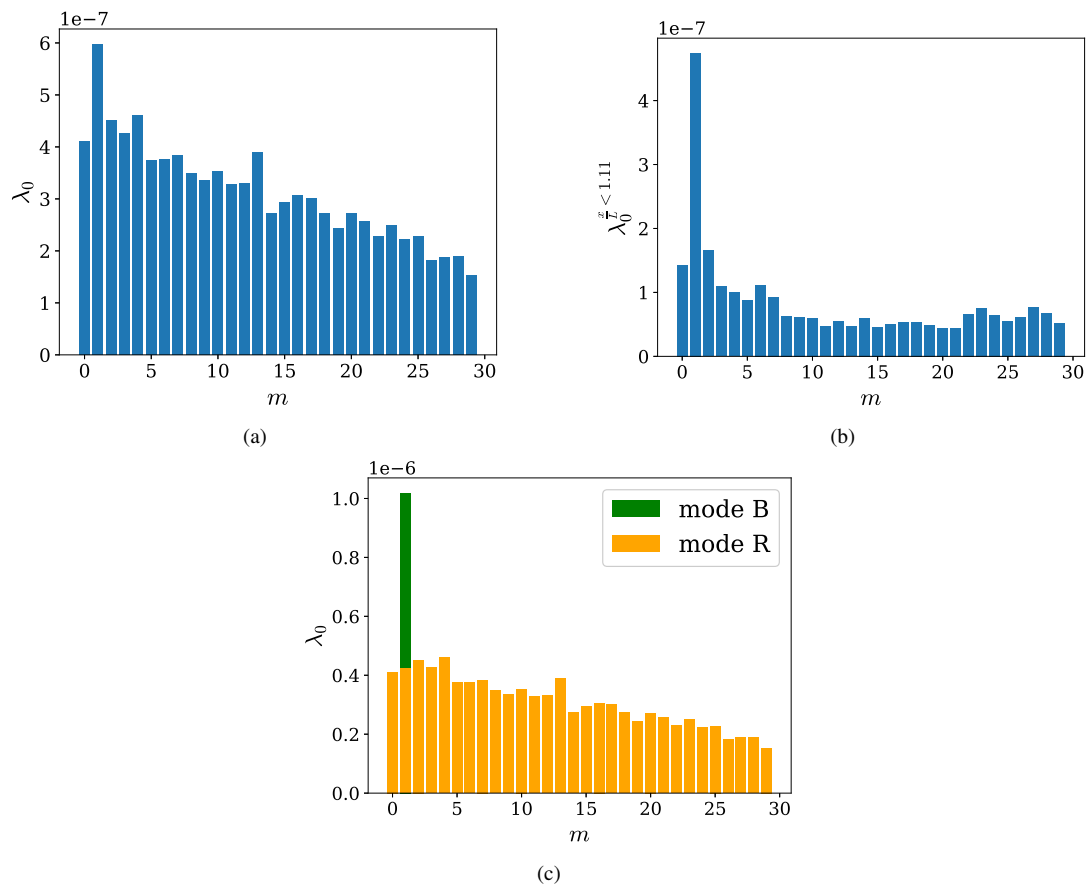


Fig. 6 Energy contained in the leading POD mode. (a): when the optimization is conducted on the full domain, (b): restrained on the region upstream from the reattachment point. (c) : for the full domain but showing the contribution of the two most energetic modes for $m = 1$.

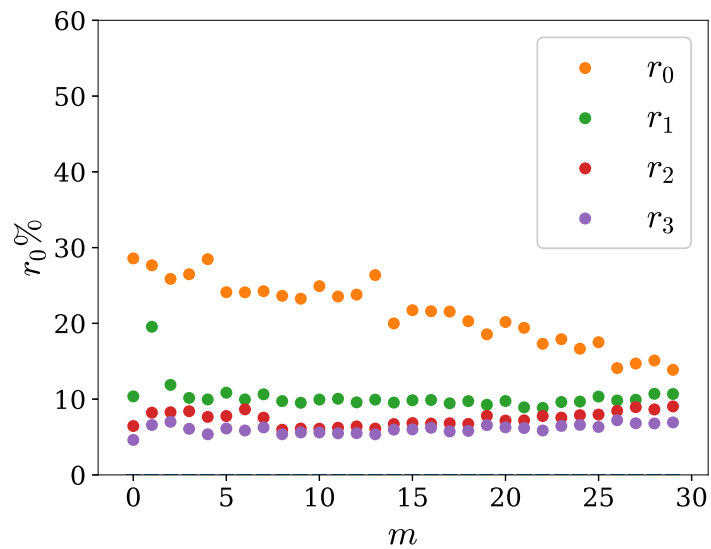


Fig. 7 Percentage of energy contained in the first 4 POD modes against the wavenumber (POD modes computed from the full domain).

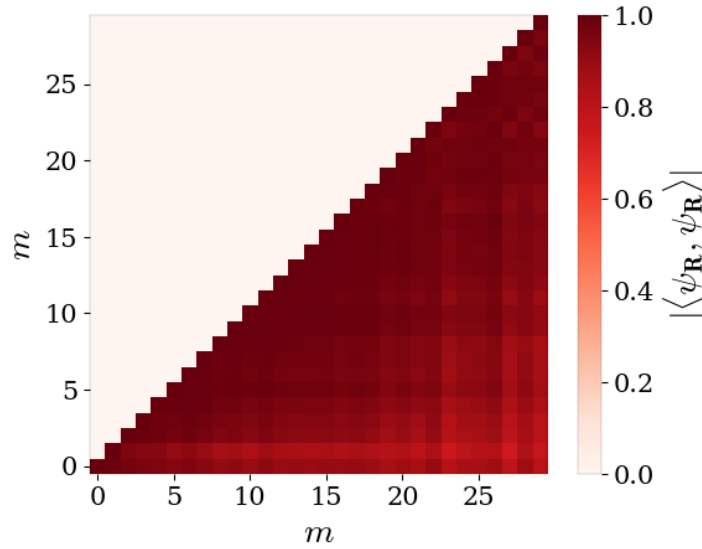


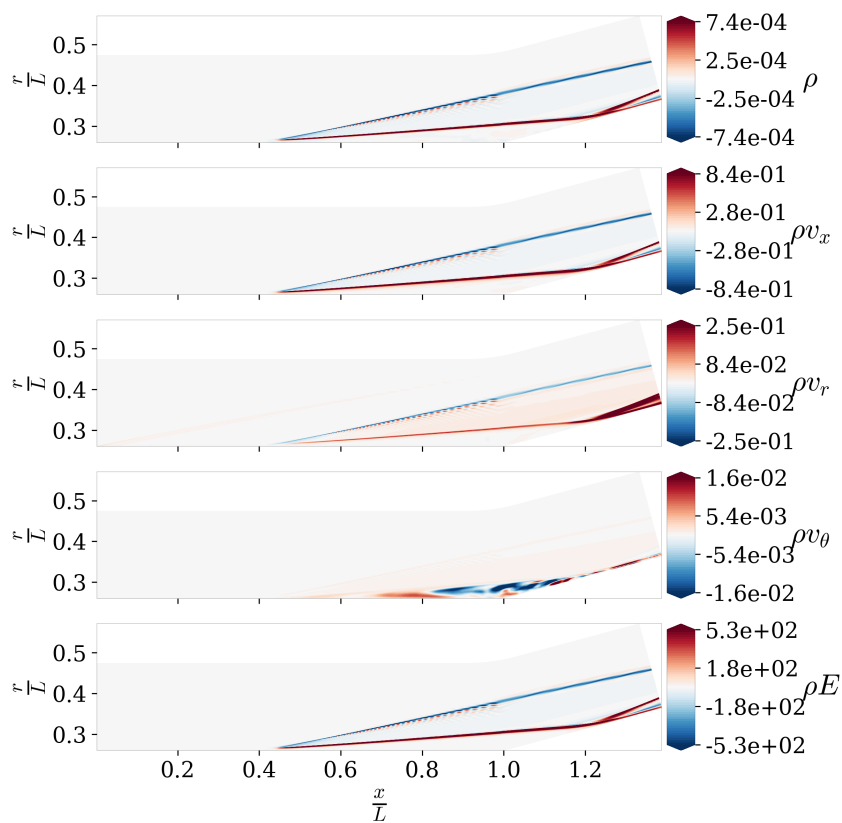
Fig. 8 Alignment coefficient between the POD modes identified as mode R for different wavenumbers. Due to the symmetry $|\langle \Psi_R^{m=a}, \Psi_R^{m=b} \rangle| = |\langle \Psi_R^{m=b}, \Psi_R^{m=a} \rangle|$, only half of the map is displayed.

Nevertheless, the previously discussed figures only represent the energetic level of the leading POD mode and ignore the lower-ranked modes that may still significantly contribute to the dynamics. Figure 7 presents the percentage of energy contained by the four dominant POD modes for each wavenumber. Overall, there is a clear separation between the leading POD mode and lesser-ranked modes for all wavenumbers except $m = 1$, where the second mode also contains a significant level of energy (it contains more than 22% of the energy at $m = 1$ while it is less than 10% for most of the higher wavenumber). This second POD mode at $m = 1$ aligns well with other R-modes at higher wavenumber (see figure 8), indicating the coexistence of mode B and R at $m = 1$. At higher wavenumbers, the flow is clearly dominated by a single mode, identified as mode R. Lesser rank modes are clustered to significantly lower energetic levels and are therefore not studied here. To summarize those findings, the energetic content of modes B and R against wavenumber is presented in figure 6 (c).

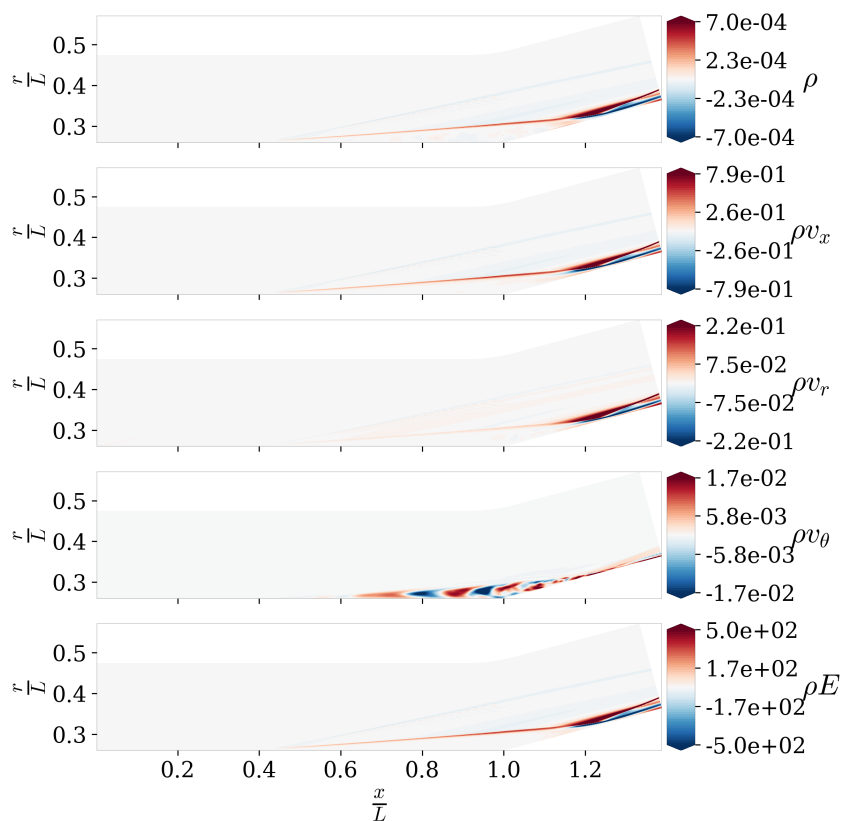
Figure 9 presents the spatial shape of modes R and B. Mode B displays strong field variations in the separation shock and mixing layer. For that reason, the interpretation of its energetic content is not straightforward: the displacement of the shock causes a strong variation in most of the fields because of both the amplitude of the motion, which is a feature of the mode, and the jump relation across the shock, which is not. Thus, the energetic content of the mode may not be fully attributed to its dynamic. Note that since the modes are computed by solving an eigenvalue problem, they are defined up to a complex multiplicative constant, and therefore their phase is arbitrary. The spatial shape of the modes confirms the results obtained from figure 6: mode B is located mainly in the mixing layer and the separation shock, while mode R is strong in the reattachment region (even if it is still present in the recirculation region, mostly for ρv_θ).

In the present study, the main drawback of this POD-based analysis is that it provides very little information on the temporal frequency (which is only known to be lower than $S_{L_{sep}} = 0.86$). It is impossible to assess if the modes are steady or not. If they oscillate, their frequency is likely too low to be properly characterized from the available high-fidelity data. It is worthy to note that this is not a drawback of the POD method itself, but a limitation stemming from the available data of the present study. As stated in section 2.3, the physical time that has been computed is too short compared to the mode frequency to allow for a correct interpretation of the temporal evolution of the mode.

Fortunately, one may obtain that information from the linearized Navier-Stokes operator. As discussed in section 2.4, and supposing that modes R and B are self-sustained (*i.e.* absolute) instabilities of the flow, the operator should display eigenmodes whose spatial structure would match that of the POD modes. Once such modes are found, the stability analysis directly provides their frequencies. As said in section 2.4, the modes are likely to have a growth rate near zero (but they can be stable or unstable). Therefore, we focus on the least stable/unstable modes in the following.



(a)



(b)

Fig. 9 (a): leading POD mode at $m = 1$, the mode corresponds to the identified mode B, (b): second-ranked POD mode at $m = 1$, the mode corresponds to the identified mode R. The modes are extracted from the full domain.

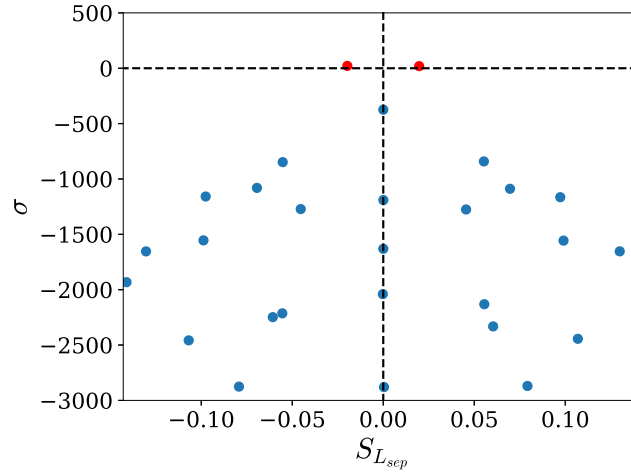


Fig. 10 Eigenvalues of the linearized operator for $m = 1$, the red dots are the two conjugate eigenvalues linked with mode B.

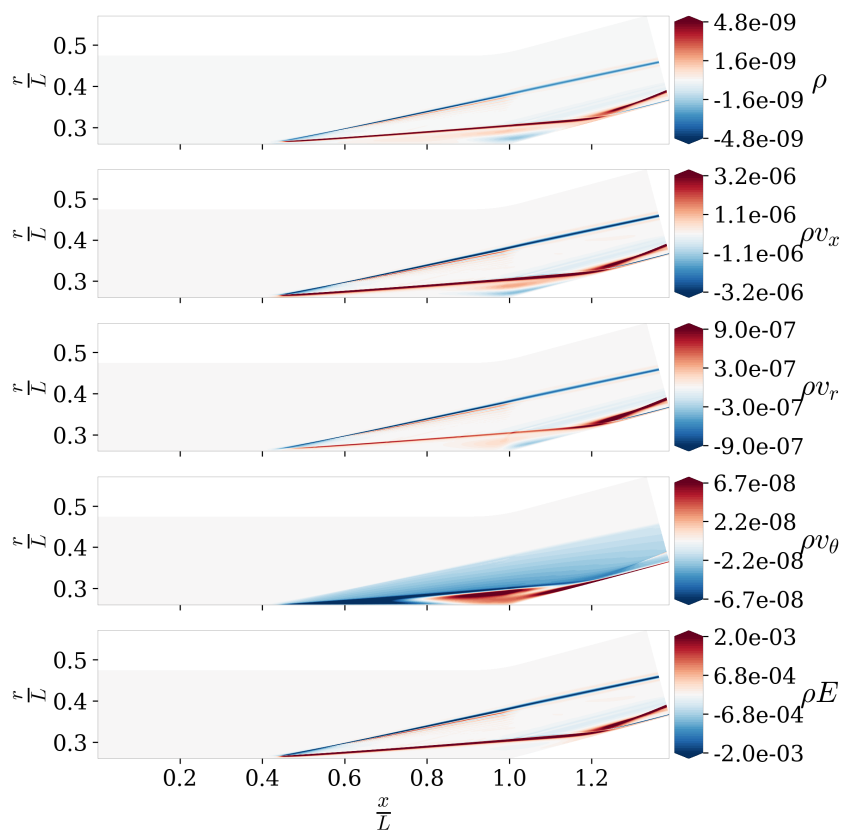
3.2 Spatio-temporal characterization of mode B

This section aims at characterizing the dynamics of mode B by analyzing the linearized Navier-stokes operator about the mean flow. The study will be conducted for $m = 1$. As explained in section 2.4, if mode B is a self-sustained instability of the flow, the stability eigenspectrum should display a mode with a near-zero growth rate and a spatial structure matching that of figure 9 (a). Then, the results of the stability analysis should provide information about the temporal behavior of this unsteadiness.

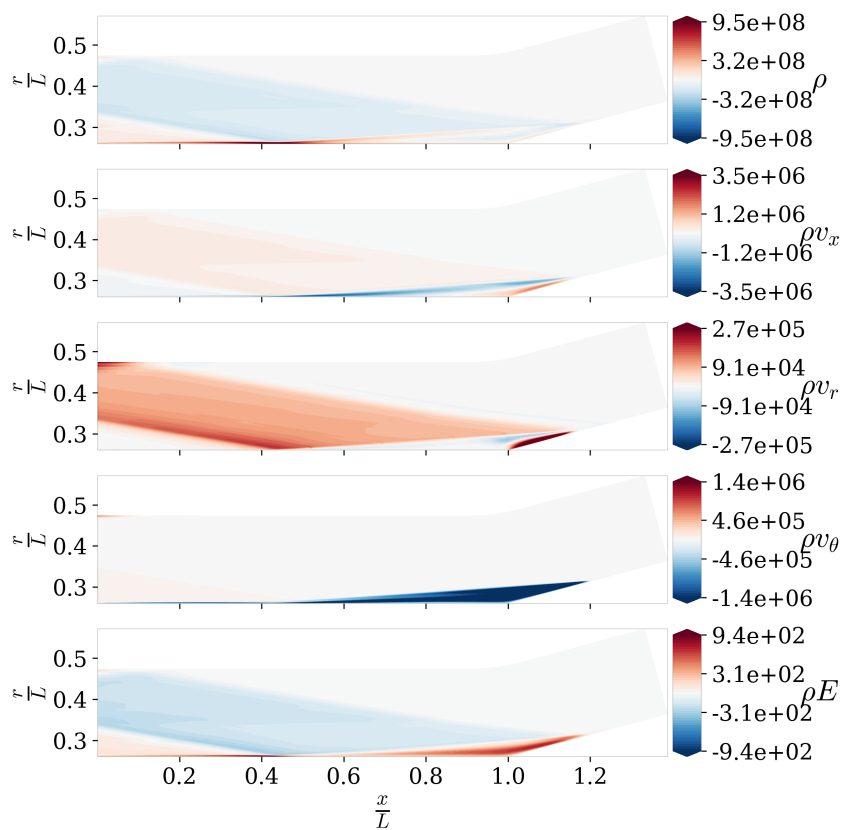
Figure 10 presents the eigenspectrum of the linearized operator for $m = 1$, showing a marginally unstable unsteady mode (and its complex conjugate). We will show that this mode corresponds to mode B identified previously. The mode pulsates at $S_{L_{sep}} = 0.019$ (110Hz). This result should, however, be taken with caution, as the averaging time of the mean flow used for this stability analysis is of the same order of magnitude than the pulsation of the mode. In the following, we still investigate the physics of the mode, as interesting parallel can be made with the existing literature. A parallel can already be made here with the reviews of Clemens *et al.* [24] and Pipponiau *et al.* [22] for shock wave-turbulent boundary layer interaction. The Strouhal numbers in those reviews are very close to the one found here: they report a value $S_{L_{sep}} = 0.025$ for a Mach 5 compression ramp, and for high-supersonic interactions (Mach 3), a range from 0.02 to 0.05 [24]. Values around $S_{L_{sep}} = 0.03$ seem to be typical for shock unsteadiness in turbulent SBLI [22,46,23]. This may point toward a common phenomenon between the present paper and these previous studies for mode B. References [47,22] have proposed a physical scenario that drives the shock unsteadiness for shock wave-turbulent boundary layer interactions. This scenario involves a self-sustained instability driven by the mass advection from the bubble by the mixing layer, which is then replenished at a much slower time scale in the reattachment region. This mode is also documented to create a bubble breathing (expansion/contraction motion) where the separation and reattachment points move in opposite directions [24].

However, the consistency between the Strouhal number from Clemens *et al.* [24], Pipponiau *et al.* [22], and the present numerical study may appear somewhat surprising since shock-turbulent BL interaction and shock-transitional BL interactions lead to entirely different bubble aspect ratios, especially for the recirculation length. Despite these drastically different conditions, the characteristic time of the unsteadiness scales with the bubble length, which confirms that L_{sep} is indeed the correct length scale involved in the physical mechanism at play. Explanations on this good match, despite the very different nature of the flow, are provided in section 3.3.

Figure 11 presents both the direct and adjoint mode linked to the marginally unstable eigenvalue. The direct mode can be compared to the dominant POD mode at $m = 1$ (see figure 9 (a)) to see that their spatial structure is very similar. The modes are mainly present in the separation shock, the mixing layer, and the reattachment region, the separation shock being in phase opposition compared to the mixing layer and reattachment. The agreement with mode B is confirmed by the value of the alignment coefficient between the POD and stability mode (see equation (1)) restricted to the relevant zone (*i.e.*, the bubble upstream of the reattachment, here $0.4 < \frac{x}{L} < 1.11$). Here, the value obtained is 0.91. This good alignment confirms the link between the stability mode and the POD mode. Then, the adjoint mode represents the



(a)



(b)

Fig. 11 (a): Unstable mode (eigenvector) linked with the marginally unstable eigenvalue at $m = 1$ for the direct operator. (b): same figure as (a) but for the adjoint operator.

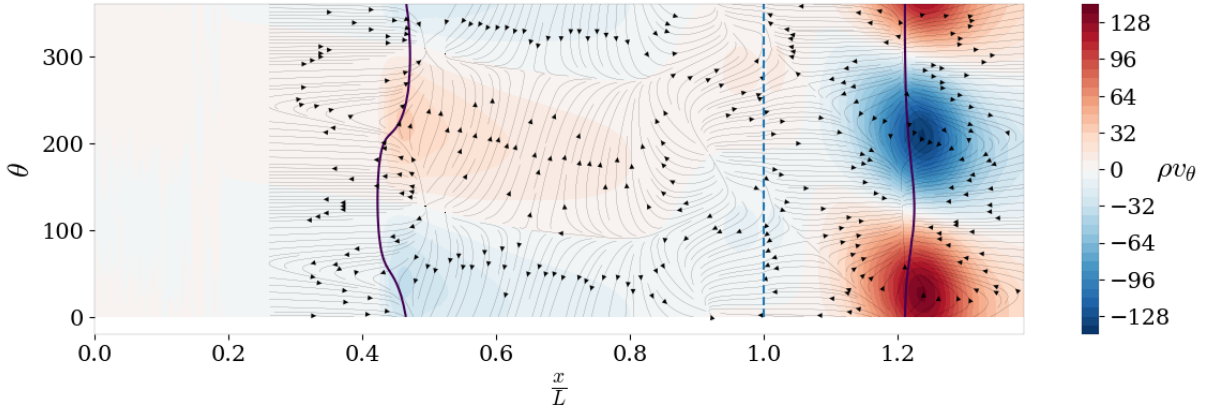


Fig. 12 Impact of the mode B at $m = 1$ on the limit of the recirculation region (black line), azimuthal momentum (colormap) and unstable mode streamlines (arrows) in the first cell above the wall. The dashed line represents the limit between the cylinder and the flare.

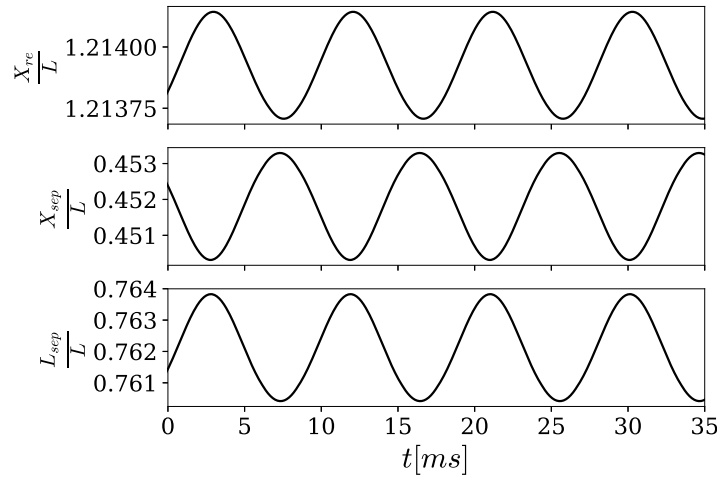


Fig. 13 Temporal evolution of the reattachment position (up), separation position (middle) and separation length (down) for a given azimuthal position. The amplitude and phase of the mode are coherent between the sub-figures but are arbitrary.

optimal perturbation that would excite mode B. In the following, it will be used to compute the wavemaker, *i.e.* the spatial zones responsible for the unsteadiness, through a structural sensitivity analysis [44].

Figure 12 presents the near-wall signature of the unstable mode B (at $m = 1$). It shows that the induced deformation of the separation and reattachment lines (obtained by superimposing the mode to the base flow) are in opposed directions. Thus, the mode corresponds to a "breathing" of the bubble. This is further illustrated by figure 13, which presents the temporal evolution of the separation and reattachment locations for a given azimuthal position, and shows that the bubble is successively expanding and shrinking. This result is reminiscent of the work of Nichols *et al.* [23], who already established a link between the "breathing" motion of the recirculation region and a global stability mode for turbulent SBLI through a mean flow stability analysis conducted on LES data.

The streamlines from figure 12 also show that the mode is responsible for fluxes of mass in and out of the bubble near the reattachment point. There are also signs that the separation and reattachment line undulations are linked with stream-wise momentum benefit or deficit, pushing them upstream or downstream depending on the position. When animated in time, mode B is found to be rotating in the azimuthal direction.

3.3 Physical mechanism driving mode B

The previous stability results point to a physical scenario for mode B that is somewhat comparable to that of [22]: the mixing layer advects information downstream, and the bubble advects information upstream in the near-wall region at a slower rate. The structural sensitivity of the mode (see section 2.4) provides insights on the underlying physical mechanism by revealing the locations responsible for the instability (*i.e.* the wavemaker). Figure 14 shows that the mode displays high sensitivity values in the mixing layer, in the near-wall region, near the separation point, and in the shock. On the contrary, the sensitivity values are low near the reattachment point. Interestingly, the local sensitivity maxima clearly draw a loop in the recirculation region, which follows streamlines of the mean flow. This loop is highlighted in figure 14 by a blue path of arrows for the downstream convection by the mixing layer and a red path of arrows for the near-wall upstream convection by the recirculation region. The travel time of the fluid along the loop is approximately 4.4ms (0.2 ms for the blue path, 4.2ms for the red path), corresponding to a dimensionless frequency of $S_{L_{sep}} = 0.039$. As such, the temporal period of the mode corresponds almost exactly to twice the time for the flow to go through this loop.

In the following, we propose a hypothetical instability scenario that may explain the factor 2 between the recirculating time and the period of the mode. First, let us start from an infinitesimal oscillating perturbation in the separation region (as it is the most sensitive region) at a frequency of $S_{L_{sep}} = 0.019$. Let us assume, for instance, that this disturbance is initiated by an upstream motion of the separation shock (see figure 13). Due to this motion, the boundary layer separation occurs earlier along the body, causing an increase in the separation length. In addition to that, the separation angle, defined as the angle between the dividing streamline and the cylinder at the separation point (see figure 15), increases as shown in figure 16. Thus, the separation shock becomes stronger, causing an increase in the adverse pressure gradient, making the separation of the boundary-layer stronger. This change in separation length and strength causes the bubble to be oversized compared to its equilibrium size (the mean separation size). The timescale associated with this change of flow topology corresponds to the advection time along the blue downstream path (*i.e.* 0.2ms).

As proposed by Pipponiau *et al.* [22], the change in recirculation bubble topology leads to a change in upstream mass flow from the reattachment region to sustain the mean separation size. However, in the present case, the initial change in topology is not caused by the vortex shedding in the mixing layer (as it is still laminar) but by a motion of the shock. From Pipponiau *et al.* [22], a physical hypothesis for the change in incoming mass flux in the reattachment region is linked with the flapping of the mixing layer. An analogy could be made here by looking at the impact of the mode on the reattachment angle α_{re} between the dividing streamline and the flare at the reattachment point (see figure 15). One may expect that when the mixing layer impacts the flare with a lower reattachment angle, more flow goes downstream towards the reattachment region, and less flow recirculates upstream (in the extreme case where this angle is null, all the flow goes downstream). As shown in figure 16, the reattachment angle indeed varies with the size of the bubble.

Therefore, one may propose the following instability scenario. When the bubble size increases, the reattachment angle decreases. Consequently, a deficit in upstream mass flow appears near the reattachment, eventually convected up to the separation point along the red path. Given the 4.2ms (half a period of the mode) travel time along this path, the mass flow deficit reaches the separation point after half a period of the initial oscillation, during the downstream-motion phase of the shock. This reinforces the motion of the initial disturbance by pulling the shock even further downstream. The same holds for an initial downstream motion of the shock, except that it leads to a shrinking of the bubble, an increase in the reattachment angle, and a mass surplus going upstream. This process will then continuously amplify the motion of the separation point until non-linear saturation stops it.

Several links exist between this hypothetical scenario and observations of Debieve et Dupont [20], who experimentally studied the dynamics of a separated turbulent SBLI. First, they noted a phase shift of π (*i.e.* half a period) between the pressure signal in the shock foot and the reattachment region, which is also the case in our scenario since an upstream motion of the separation shock causes an increase and decrease in pressure at separation and reattachment, respectively, because of the change in separation and reattachment angle. This out-of-phase relationship between the separation and reattachment region is also described in the work of Agostini *et al.* [19]. They also reported a negligible time delay between the shock motion and the bubble motion compared to the "shock timescale". In the present scenario, while this delay is not "faster than an acoustic propagation or convection in the streamwise direction" as they propose, the downstream advection time is still less than a twentieth of the mode period. They also documented the absence of correlation of the shock motion with upstream perturbations coming from the boundary layer, supported in the present study by the negligible structural sensitivity values in the boundary layer.

It is important to highlight that, contrary to what most of the existing papers propose, this bubble instability is here inherently three-dimensional as there are no marginally stable nor unstable modes corresponding to mode B in the linearized operator spectrum for $m = 0$. An hypotheses can be made to explain this three-dimensionality : the three-

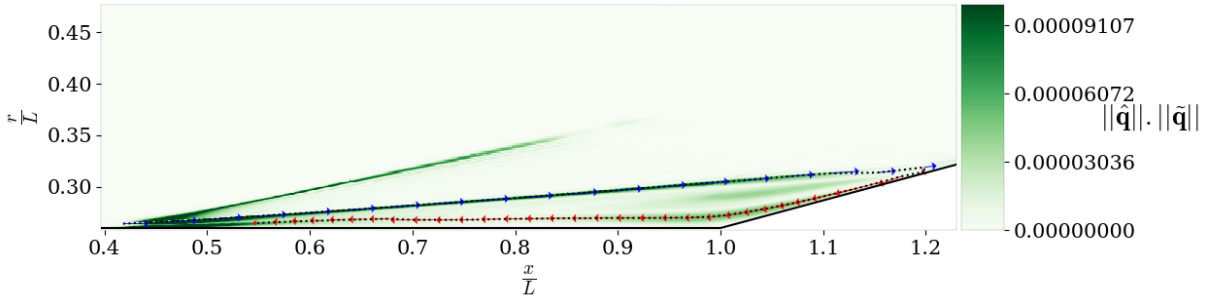


Fig. 14 Structural sensitivity of mode B for $m = 1$ along with the two information paths for the global mode deduced from local maxima of the structural sensitivity. Velocity vectors are represented along these paths (the arrows have different scales for the upper and lower paths), showing that the paths follows local mean trajectories of the flow.

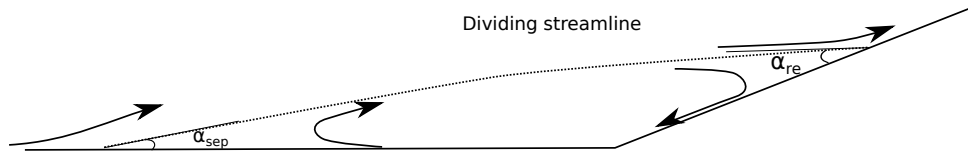


Fig. 15 Schematic showing the definition of the separation and reattachment angle.

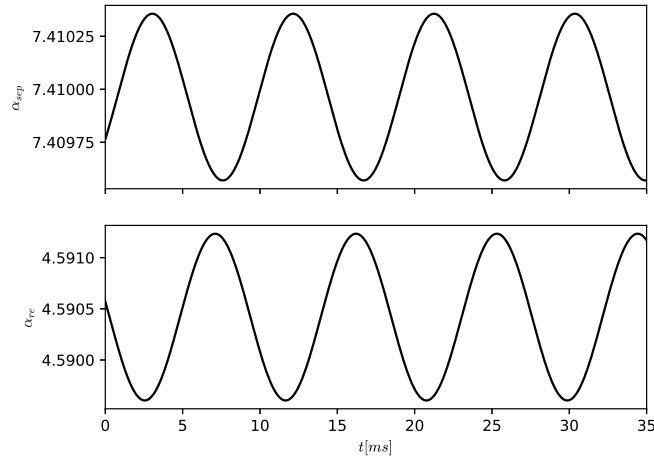


Fig. 16 Temporal evolution of the separation angle α_{sep} in degrees (up) and the reattachment angle α_{re} in degrees (down), which is defined as the angle between the dividing streamline and flare at the reattachment point computed from the superposition of the mode to the mean flow. The amplitude and phase of the mode are coherent between the sub-figures and with figure 13 but are arbitrary.

dimensionality of the perturbation may be a condition on its unsteadiness (and thus on its self-sustainability): as soon as the shock perturbation is 3D, there is an azimuthal unbalance in the pressure distribution, leading to an azimuthal motion of the separation shock perturbation. Then, the azimuthal travel of the shock-wave perturbation just has to synchronize with the bubble retro-action (*i.e.* to be of period T) to yield amplification of the shock motion. However, further work is required to conclude whether this instability could exist in a two-dimensional form, and if not, why.

3.4 Spatio-temporal characterization of mode R

This section aims at using a global stability analysis to characterize the mode identified as mode R. It focuses on $m = 5$ to discuss the results since it is one of the wavenumbers where a mode of type R strongly dominates the dynamics. But the observations/conclusions below hold for all wavenumbers for $m \in [4, 17]$. The existence of mode R for $m < 4$ and $m > 17$ is discussed in section 3.5.

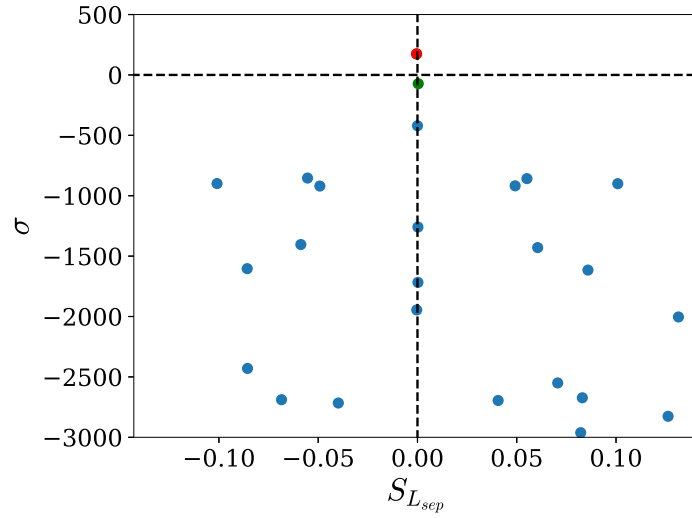


Fig. 17 Eigenvalues of the linearized operator for $m = 5$, the red and green dot are the eigenvalues linked with mode R (R-1 and R-2 respectively).

Figure 17 (a) presents the eigenspectrum of the linearized operator for $m = 5$. Contrary to the spectrum for $m = 1$, there are neither unstable nor marginally stable pairs of unsteady eigenvalues. Instead, there are two eigenvalues near the real axis, both quasi-steady, one displayed as a red dot and the other shown as a green dot. They will be called in the following mode R-1 and mode R-2, respectively.

A priori, mode R could stem from both of those eigenvalues. However, a study of their spatial structure shows that they significantly differ from the POD mode: the alignment coefficients with the POD mode in the entire domain are 0.15 and 0.32 for R-1 and R-2 eigenmodes, respectively. Figures 18 and 19 illustrates these differences by comparing the spatial shape of the eigenmodes to the POD mode. Even if figures 18 (a) and (b) show that both modes R-1 and R-2 are mainly present in the reattachment region, there are still some significant discrepancies between them and the POD mode, especially for the fluctuations inside the bubble, which strongly differs.

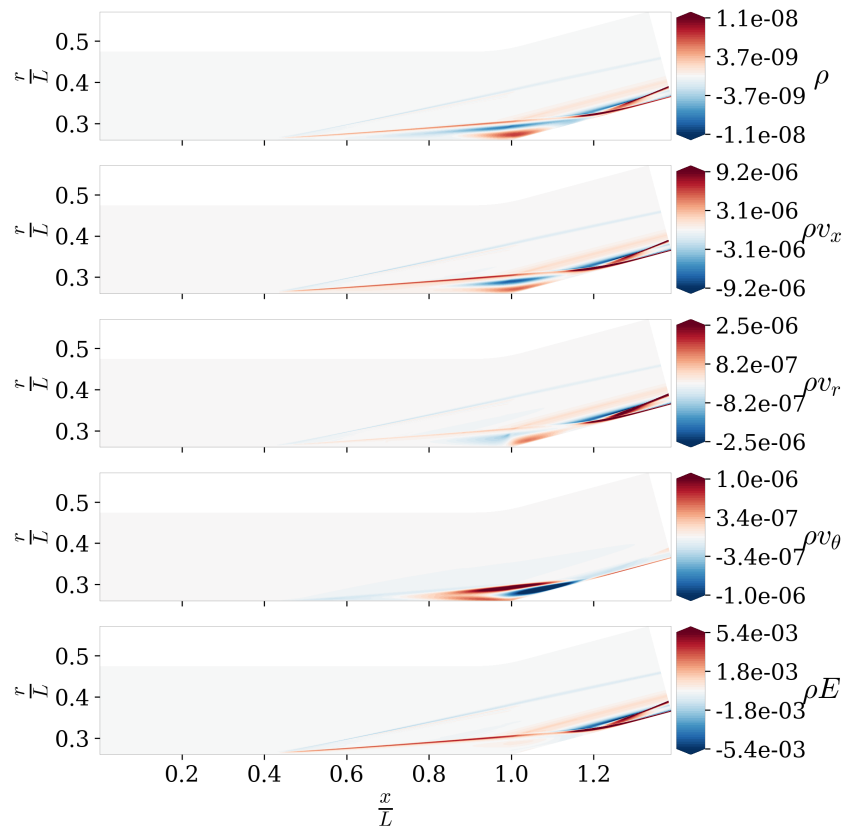
A hypothesis could then be that these two stability modes are present in the simulation and that the POD mode results from their interaction. A way to check this assumption is to investigate the low-amplitude region of the modes. In this region (*i.e.* in the recirculation region), non-linear interactions of the stability modes should be weak, such that the resulting mode R should appear as a linear combination of modes R-1 and R-2. However, this is not true in the reattachment region since non-linear terms dominate this high-amplitude region. To confirm that hypothesis, one can check if the POD mode belongs to the linear span of the two stability modes. This may be done by using a least-square method to find the best linear combination of R-1 and R-2 modes matching the POD mode in the recirculation region ($0.4 < \frac{x}{L} < 1.11$):

$$(\alpha, \beta) = \underset{\tilde{\alpha}, \tilde{\beta}}{\operatorname{argmin}} (|\tilde{\alpha}\hat{q}_{R-1} + \tilde{\beta}\hat{q}_{R-2} - \Psi|^2) \quad (2)$$

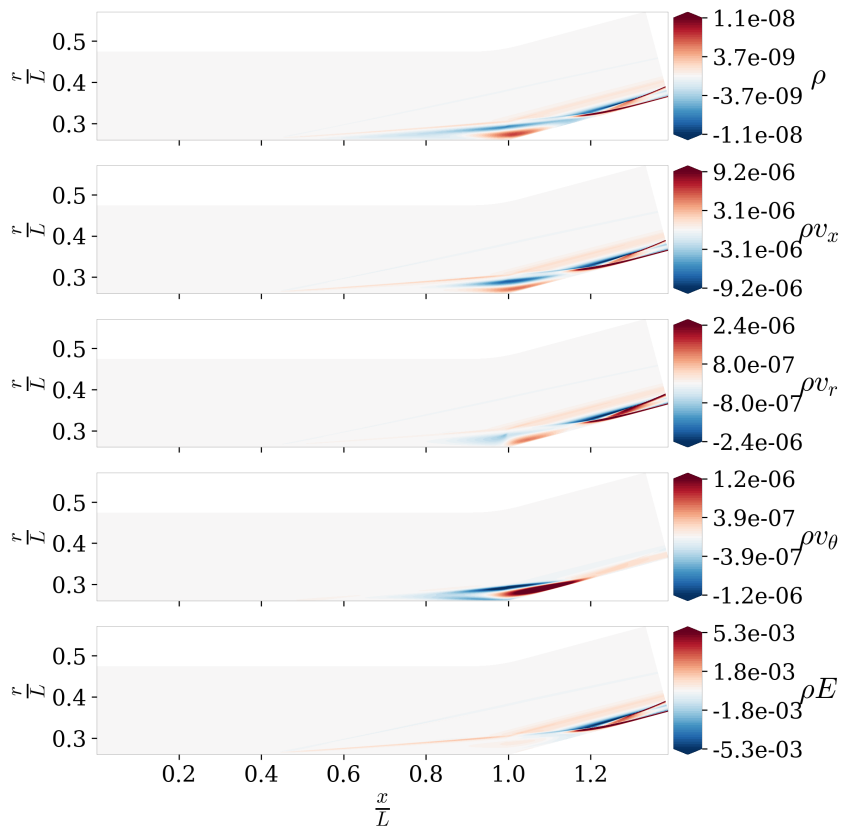
This optimized combination $\hat{q}_{R-(1+2)} = \alpha\hat{q}_{R-1} + \beta\hat{q}_{R-2}$ has an alignment coefficient (see equation 1) with the POD mode of 0.95 (against 0.62 for mode R-1 alone and 0.2 for mode R-2 alone). This means that while the POD mode is not aligned with either of the stability modes, it belongs to the subspace spanned by these two modes. This result confirms that mode R is due to the interaction of the linear global modes R-1 and R-2.

3.5 Physical mechanism driving mode R

Now that mode R is characterized as a quasi-steady mode due to the interaction of two global instabilities, the question of its physical origin remains. Figure 20 presents the evolution of the growth rate and frequency of mode R-1 and R-2 against the wavenumber. R-1 mode display a destabilization (increase in growth rate) for increasing wavenumbers up to 10, followed by a growth rate decrease. While keeping in mind the limitations of the interpretation of the growth rate mentioned in section 2.4, it is interesting to note that a similar quasi-steady unstable branch is already documented in the literature (albeit for a base flow stability analysis) [12, 13]. The present study confirms that this mode exists in



(a)



(b)

Fig. 18 (a): Unstable mode R-1 (eigenvector) for the marginally unstable eigenvalue at $m = 5$. (b): Stable mode R-2 for the marginally stable eigenvalue at $m = 5$.

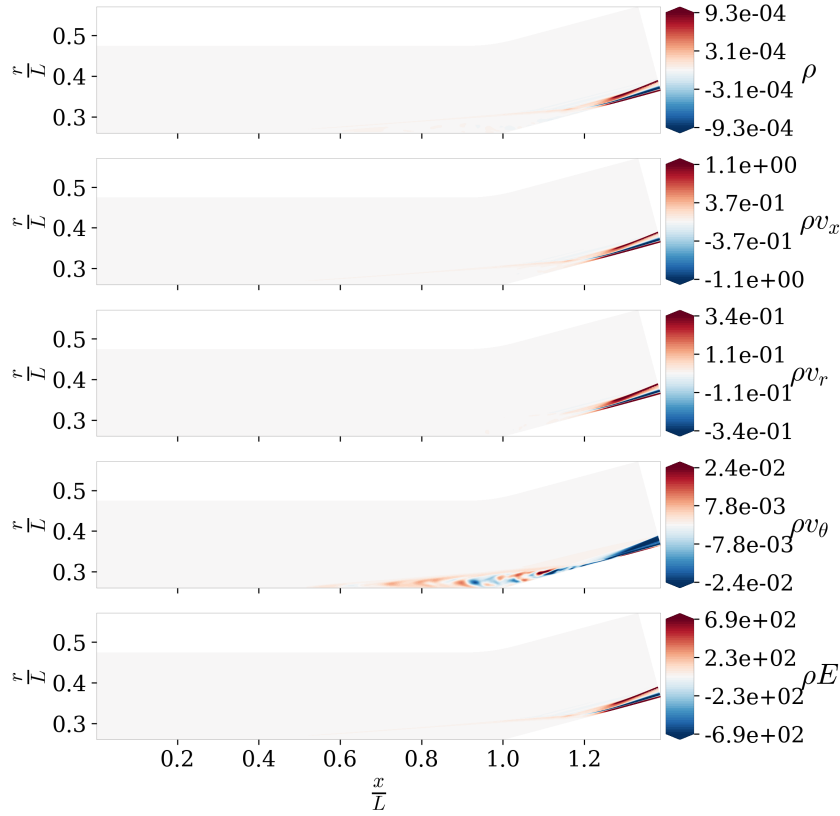


Fig. 19 Leading POD mode at $m = 5$ extracted from the full domain.

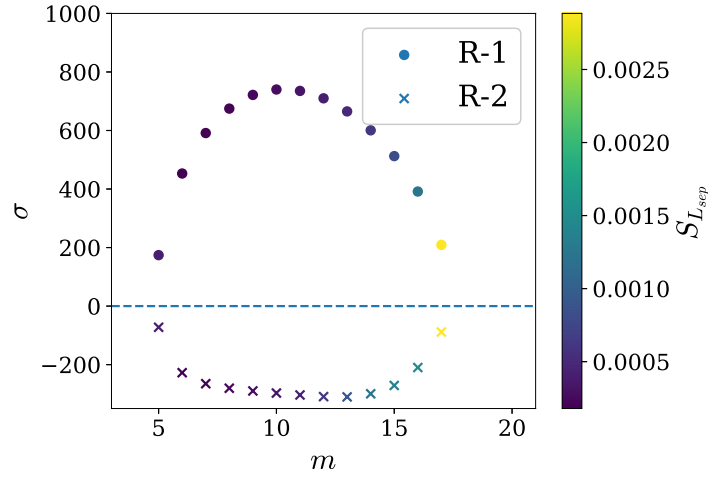


Fig. 20 Evolution of the growth rate and frequency of mode R-1 (o) and R-2 (x) against wavenumber.

transitional flows and can be found by a mean flow stability analysis. The behavior of mode R-2 mirrors that of mode R-1, with first a decrease in growth rate until $m = 13$ then an increase until $m = 17$. The frequencies of both modes R-1 and R-2 are equal at every wavenumber and are slightly increasing with wavenumber, indicating that they may relate to a similar physical mechanism. It is also worth mentioning that while mode R-2 has a negative growth rate, it is almost always closer to the real axis than mode R-1. Therefore, it has no reason to be less relevant (see section 2.4). Both of the branches disappear for wavenumbers $m > 17$ and $m < 4$. The presence of mode R for $m < 4$ in the QDNS that was

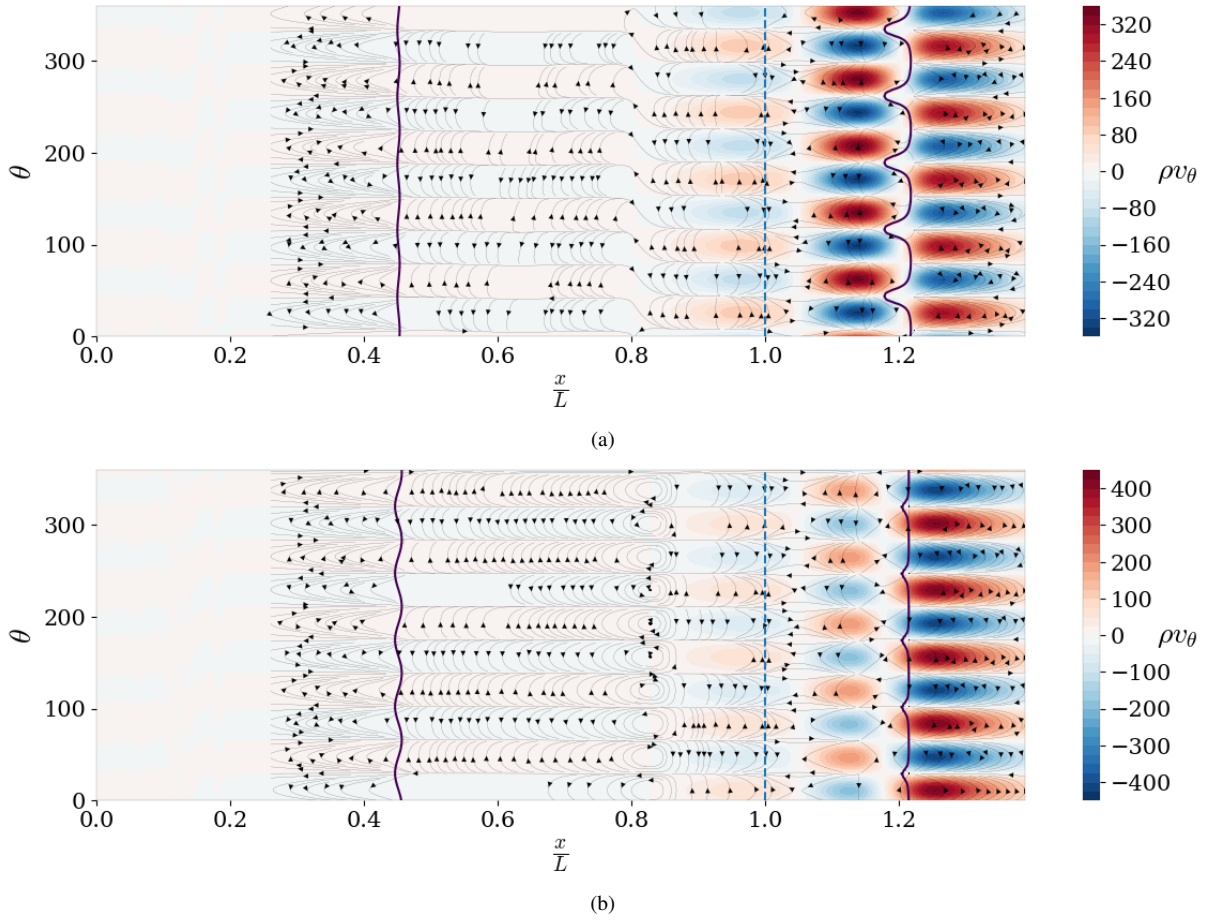


Fig. 21 (a): Impact of the mode R-1 at $m = 5$ on the limit of the recirculation region (black line), azimuthal momentum (colormap) and mode streamlines (arrows) in the first cell above the wall. (b): same figure as (a) but for the mode R-2 at $m = 5$. The dashed line represents the limit between the cylinder and the flare.

presented in section 3.1 cannot be explained by the linear growth and interaction of modes R-1 and R-2. Therefore, it may be due to the non-linear interaction of several of R-modes at higher wavenumbers ($m > 4$) which can redistribute energy toward smaller wavenumbers. The same holds for $m > 17$.

Let us now discuss the mechanism leading to the self-sustained instability proposed by Hildebrand *et al.* [12], which may be relevant for R-1 and R-2 modes. Their scenario relies on the apparition of streamwise vortices in the separated region, creating a spanwise undulation in the reattachment line (through the redistribution of streamwise momentum). Because of the feedback through the recirculation region, this undulation leads to the apparition of corrugation in the base of the separation shock. Then, this amplifies the streamwise vortices, closing the feedback loop of the global instability mechanism.

The results presented in figures 21 (a) and (b) show that this scenario is also happening here, not only for mode R-1, but also for mode R-2. Both modes display a parietal azimuthal (spanwise) momentum signature very close to that presented by Hildebrand *et al.* [12], reminiscent of the presence of streamwise vortices in the recirculation and reattachment region. Because of the near-wall streamwise momentum deficit induced by those vortices, the reattachment line undulates. This causes the corrugation of the separation line, leading to the amplification of the streamwise vortices. The fact that both modes R-1 and R-2 seem to be caused by the same underlying mechanism may explain the frequency similitude observed in figure 20.

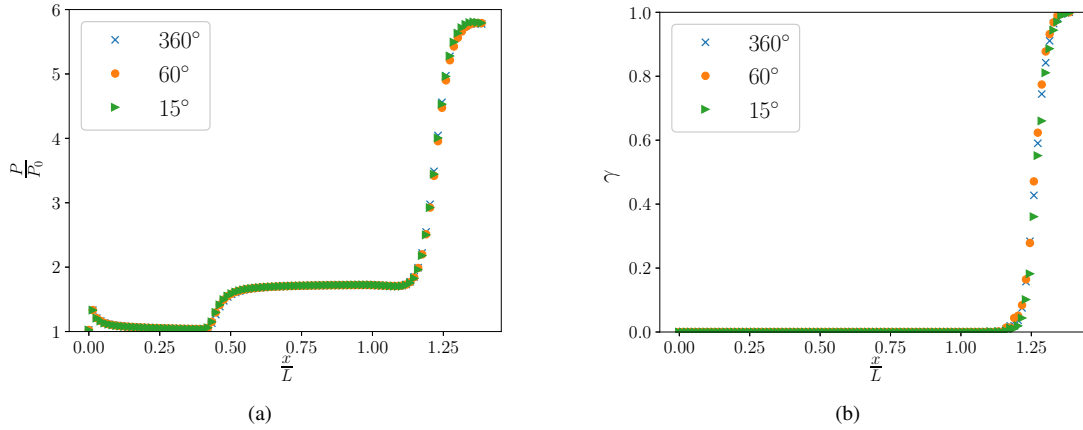


Fig. 22 Mean wall pressure distribution (a) and intermittency function (b) for the 3 different azimuthal spans of the computational domain.

3.6 Partial conclusions on the large-scale dynamics

To conclude, two large-scale modes dominate the bubble dynamics: First, a quasi-steady mode (mode R) that causes a striation in the reattachment region and which stems from the interaction of two quasi-steady self-sustained modes. Then, an unsteady mode (mode B) that causes a breathing motion of the bubble, also linked to a global instability.

A scenario leading to a self-sustained instability has been discussed for both modes. The unsteady mode may correspond to the shock unsteadiness already documented in several shockwave-turbulent boundary layer interactions cases.

4 Impact of the large scale dynamics on transition

The previous section has unveiled the low frequency, low wavenumber modes dominating the recirculation region. First, and as postulated by [6], there is a scale separation between the previously discussed dynamics and the convective instabilities leading to transition. Thus, the hypothesis that the recirculation region modes are the cause for transition is unlikely. However, this scale separation does not allow us to conclude if the bubble dynamics impacts the transition through the modification of the mean flow, which may affect the linear amplification mechanisms of the convective instabilities.

The impact of the bubble dynamics on the transitional one can be assessed by comparing the three different simulations (QDNS A, B, and C, see table 2). As explained in section 2.2, the reduction of the domain azimuthal span leads to a periodic filtering of the wavenumbers that develop in the simulations. This yields three simulations containing different global modes. First, the full domain simulation (QDNS A) contains every mode. Thus, it serves as a reference to study the impact of those modes on the flow topology and convective instabilities. Then, the simulation on the 60° domain (QDNS B) can only contain modes R, as modes of type B are energetic only for low wavenumbers filtered by the domain span (modes of wavenumber smaller than six cannot develop). Finally, the 15°-simulation (QDNS C) contains no unstable recirculation modes, since the smallest non-zero wavenumber that can develop is 24, effectively filtering mode B and mode R.

This section focuses on the difference in flow topology and transition caused by the presence, or absence, of the two unstable modes of the separated region.

First, and as presented through the wall pressure distribution in figure 22 (a), all three simulations predict the same mean-flow topology with no difference neither in the separation nor in the reattachment point location. This is a significant result given the already discussed dependence of recirculation region length on the transition to turbulence, hinting that the suppression of the bubble modes has no impact on the transition. This assumption can be confirmed by computing an intermittency function, which represents the probability of being in a turbulent spot at a given location (see the work of Narashima [48] for more details). The intermittency is computed based on pressure spectrograms following an idea of Arnal [49]. The intermittency distribution is displayed in figure 22 (b) for the three simulations. It confirms that the transition onset and the point where the flow reaches completely developed turbulence are the same for all cases.

To go further in the comparison between the three simulations, figure 23 presents wall pressure power spectral densities at different longitudinal locations; (a) is situated in the boundary layer, (b) and (c) in the separated region, and

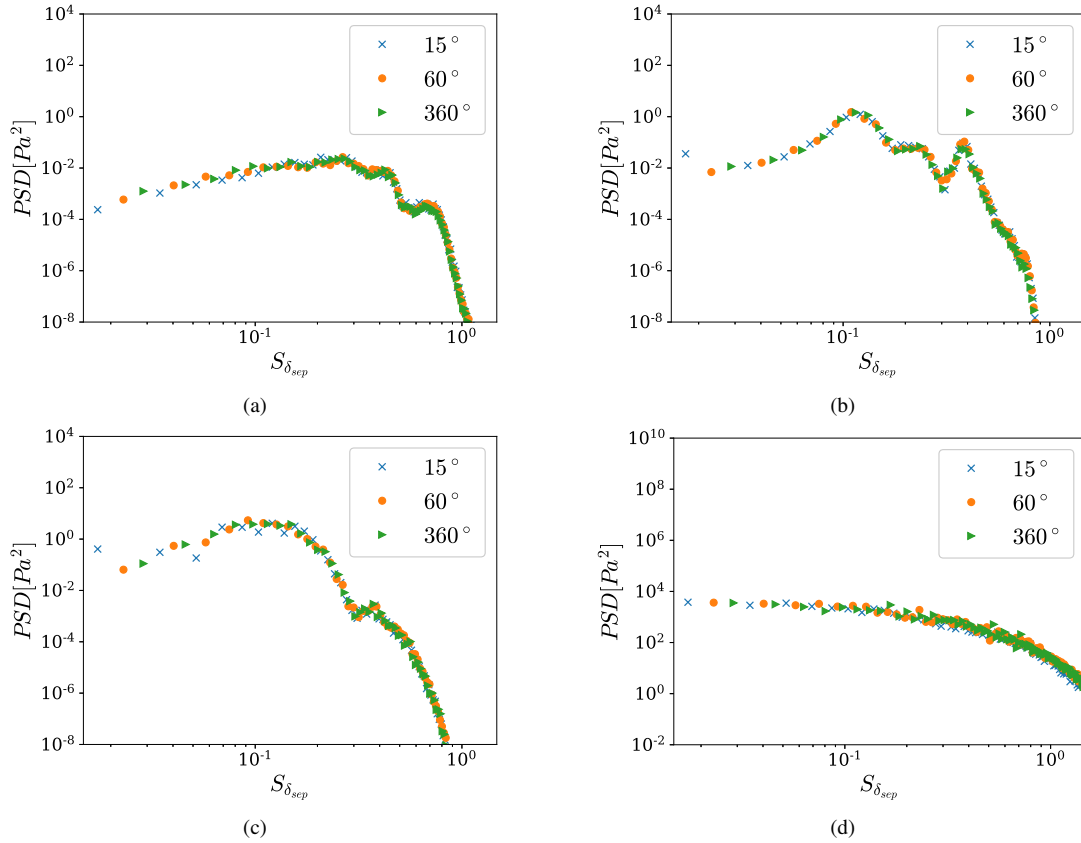


Fig. 23 Pre-multiplied wall pressure power spectral density at station: boundary layer at : $\frac{x}{L} = 0.28$ (a), separated region at $\frac{x}{L} = 0.56$ (b) and $\frac{x}{L} = 0.91$ (c), reattached region at $\frac{x}{L} = 1.33$ (d) for the 3 different azimuthal span of the computational domain.

(d) after the reattachment point. Those four figures give a good overview of the complete transitional dynamics of the flow. They all show that there is no noticeable difference between the three simulations. Mainly two different transitional instabilities can be spotted in figure 23 (a) and (b): a bump at frequencies around $S_{\delta_{sep}} = 0.4 - 0.5$, which is linked to second mode instabilities and another broad bump at lower frequencies (especially visible in figure 23 (b)), which is linked to oblique first mode instabilities. The study of the transition scenario on the 15° domain revealed that it is similar to that presented at Mach 5 by Lugin *et al.* [6] which relies on the non-linear interaction of oblique modes in the attached boundary layer to create streaks that are then linearly amplified in the separation and reattachment region. Both of those instabilities have the same wall pressure fluctuation signature for all three QDNSs. Thus, they are unaffected by the bubble dynamics.

From the results presented in this section, one can conclude that the low-frequency/large-scale motion of the recirculation region, albeit present in this flow, has no impact on the transitional instabilities, the overall transition process, and most importantly, the mean topology of the flow. This also implies that transition scenarios based on absolute instabilities of the bubble such as proposed by Cao *et al.* [14] become irrelevant in cases with significant free-stream perturbations such as studied here. Computations on a reduced domain (at least down to 15°) can fully predict the correct flow topology and high-frequency dynamics.

5 Conclusion

A complete study of the dynamics of a strongly separated hypersonic shockwave-transitional boundary layer interaction has been conducted. First, a QDNS excited by a generic inlet noise has been performed on a full (360 degrees) domain. This simulation has been post-processed using time-filtered data through POD to unveil the self-sustained dynamics of the recirculation region. The physical scenarios behind those modes were then studied through a mean-flow global

stability analysis. An assessment of the information brought by the study of the Navier-Stokes operator linearized around the mean flow was presented, with a critical point of view on the interpretation of the growth rate.

The flow is mainly dominated by two coexistent coherent modes. First, a quasi-steady mode that mainly exists in the reattachment region (mode R). This mode is linked to an already documented scenario [12] that relies on the apparition of streamwise vortices in the recirculation region, which can amplify themselves through the deformation of the bubble. Secondly, an unsteady mode causing the breathing of the bubble through a back-and-forth motion of both the separation and reattachment points (mode B). A new self-sustained instability scenario for the shock unsteadiness has been proposed. This hypothetical scenario is linked with a feedback loop inside the recirculation bubble, with information being convected downstream by the mixing layer and upstream by the near-wall region of the recirculation region.

Then, the impact of the bubble dynamics on the transitional mechanism has been studied through two other QDNSs with spatial filtering of the bubble modes. Those simulations showed that, for a flow with significant amount of free-stream noise, the bubble dynamics has no impact on the transitional instabilities. This is a significant result because it means that crucial design parameters such as heat-flux, transition onset, and separation size can be accurately simulated on a reduced domain, leading to a significant gain in the computational cost. Adding to that the possibility to use QDNS instead of DNS for those cases, as already demonstrated by Lugrin *et al.* [6], it leads to a major reduction of the numerical complexity of such simulations for transitional SBLI (more than two orders of magnitude), without losing accuracy on the prediction of key design factors.

Acknowledgements This work was supported by the French Alternative Energies and Atomic Energy Commission (CEA) under the grant CEA 4600334751. The QDNS A and B (see table 2) were performed on the OCCIGEN supercomputer at CINES under the GENCI allocation A0072A11041. The authors thank Julien Dandois for its comment on the article. The datasets generated during and/or analysed during the current study are available from the corresponding author on reasonable request.

Conflict of interest

The authors declare that they have no conflict of interest.

References

1. H.F. Fasel, A. Thumm, H. Bestek, in *Fluids Engineering Conference* (Publ by ASME, 1993), pp. 77–92
2. N. Adams, L. Kleiser, in *5th International Aerospace Planes and Hypersonics Technologies Conference* (1993), p. 5027
3. K.J. Franko, S.K. Lele, *Journal of Fluid Mechanics* **730**, 491–532 (2013)
4. K.J. Franko, S. Lele, *Physics of Fluids* **26**(2), 024106 (2014). URL <https://doi.org/10.1063/1.4864337>
5. C. Hader, H.F. Fasel, *Journal of Fluid Mechanics* **847** (2018)
6. M. Lugrin, S. Beneddine, C. Leclercq, E. Garnier, R. Bur, *Journal of Fluid Mechanics* **907** (2021)
7. O. Marxen, U. Rist, *Journal of Fluid Mechanics* **660**, 37 (2010)
8. N. Sandham, W. Reynolds, *Journal of Fluid Mechanics* **224**, 133 (1991)
9. H. Gortler, *ZAMM - Journal of Applied Mathematics and Mechanics Zeitschrift für Angewandte Mathematik und Mechanik* **21**(4), 250 (1940)
10. A. Dwivedi, G. Sidharth, J.W. Nichols, G.V. Candler, M.R. Jovanovi'c, *Journal of Fluid Mechanics* **880**, 113 (2019)
11. J.C. Robinet, *Journal of Fluid Mechanics* **579**, 85 (2007)
12. N. Hildebrand, A. Dwivedi, J.W. Nichols, M.R. Jovanovi'c, G.V. Candler, *Physical Review Fluids* **3**(1), 013906 (2018)
13. G. Sidharth, A. Dwivedi, G.V. Candler, J.W. Nichols, *Physical Review Fluids* **3**(9), 093901 (2018)
14. S. Cao, J. Hao, I. Klioutchnikov, H. Olivier, C.Y. Wen, *Journal of Fluid Mechanics* **912**, A3 (2021)
15. N.A. Adams, *Journal of Fluid Mechanics* **420**, 47–83 (2000)
16. M. Wu, M.P. Martin, *AIAA Journal* **45**(4), 879 (2007)
17. S. Priebe, M.P. Martin, *Journal of Fluid Mechanics* **699**, 1 (2012)
18. S. Priebe, J.H. Tu, C.W. Rowley, M.P. Martin, *Journal of Fluid Mechanics* **807**, 441 (2016)
19. L. Agostini, L. Larchevêque, P. Dupont, *Physics of Fluids* **27**(12), 126103 (2015)
20. J.F. Debiève, P. Dupont, *Shock Waves* **19**(6), 499 (2009)
21. E. Touber, N.D. Sandham, *Journal of Fluid Mechanics* **671**, 417 (2011)
22. S. Piponniau, J.P. Dussauge, J.F. Debiève, P. Dupont, *Journal of Fluid Mechanics* **629**, 87 (2009)
23. J.W. Nichols, J. Larsson, M. Bernardini, S. Pirozzoli, *Theoretical and Computational Fluid Dynamics* **31**(1), 33 (2017)
24. N.T. Clemens, V. Narayanaswamy, *Annual Review of Fluid Mechanics* **46**(1), 469 (2014)
25. R. Bur, B. Chanetz, *Aerospace Science and Technology* **13**(7), 393 (2009)
26. R. Benay, B. Chanetz, B. Mangin, L. Vandomme, J. Perraud, *AIAA Journal* **44**(6), 1243 (2006)
27. S. Péron, T. Renaud, I. Mary, C. Benoit, M. Terracol, in *23rd AIAA Computational Fluid Dynamics Conference* (2017), p. 3623
28. I. Mary, P. Sagaut, *AIAA Journal* **40** (2001)
29. P.R. Spalart, *International Journal of Heat and Fluid Flow* **21**(3), 252 (2000)
30. J. Lumley, *New York Academic* (1970)
31. K. Gudmundsson, T. Colonius, *Journal of Fluid Mechanics* **689**, 97 (2011)

32. A. Towne, O.T. Schmidt, T. Colonius, *Journal of Fluid Mechanics* **847**, 821 (2018)
33. J. McClellan, T. Parks, *IEEE Transactions on Circuit Theory* **20**(6), 697 (1973)
34. B.J. McKeon, A.S. Sharma, arXiv preprint arXiv:1001.3100 (2010)
35. S. Beneddine, D. Sipp, A. Arnault, J. Dandois, L. Lesshafft, *Journal of Fluid Mechanics* **798**, 485 (2016)
36. D. Sipp, A. Lebedev, *Journal of Fluid Mechanics* **593**, 333 (2007)
37. S.E. Turton, L.S. Tuckerman, D. Barkley, *Physical Review E* **91**(4), 043009 (2015)
38. C. Mettot, F. Renac, D. Sipp, *Journal of Computational Physics* **269**, 234 (2014)
39. U. Karban, B. Bugeat, E. Martini, A. Towne, A. Cavalieri, L. Lesshafft, A. Agarwal, P. Jordan, T. Colonius, arXiv preprint arXiv:2005.05703 (2020)
40. P.J. Schmid, M.F. de Pando, N. Peake, *Physical Review Fluids* **2**(11), 113902 (2017)
41. E. Paladini, S. Beneddine, J. Dandois, D. Sipp, J.C. Robinet, *Physical Review Fluids* **4**(10), 103906 (2019)
42. F. Giannetti, P. Luchini, *Journal of Fluid Mechanics* **581**(1), 167 (2007)
43. O. Marquet, D. Sipp, L. Jacquin, *Journal of Fluid Mechanics* **615**, 221 (2008)
44. P. Luchini, F. Giannetti, J. Pralits, in *IUTAM Symposium on Unsteady Separated Flows and their Control* (Springer, 2009), pp. 151–160
45. E.M. Pickering, A. Towne, P. Jordan, T. Colonius, in *AIAA Scitech 2020 Forum* (2020), p. 0999
46. E. Touber, N.D. Sandham, *Theoretical and Computational Fluid Dynamics* **23**(2), 79 (2009)
47. M. Wu, M.P. Martin, *Journal of Fluid Mechanics* **594**, 71 (2008)
48. R. Narasimha, *Modelling the transitional boundary layer* (NASA, Langley Research Center, Institute for Computer Applications in Science and Engineering, 1990)
49. D. Arnal, J.C. Juillen, *La Recherche Aérospatiale* pp. 147–166 (1977)
50. B.T. Chu, *Acta Mechanica* **1**(3), 215 (1965)
51. A. Hanifi, P.J. Schmid, D.S. Henningson, *Physics of Fluids* **8**(3), 826 (1996)
52. K.J. George, R. Sujith, *Journal of Sound and Vibration* **330**(22), 5280 (2011)
53. B. Bugeat, J.C. Chassaing, J.C. Robinet, P. Sagaut, *Journal of Computational Physics* p. 108888 (2019)
54. G. Berkooz, P. Holmes, J.L. Lumley, *Annual Review of Fluid Mechanics* **25**(1), 539 (1993)

Appendix 1 : Noise injection

This section is dedicated to the technical description of the white noise injection in the QDNSs following the procedure described in [6]. The injection is realized 4 cells downstream ($i = 4$) of the inlet boundary condition in order not to interfere with it. The form of this injection is the following :

$$\rho'[j, k] = \rho[j, k](1 + 0.01r_n[j, k]) \quad (3)$$

With r_n a random number normalized such that the root-mean-square on the whole injection plane is 1 :

$$r_n[j, k] = \frac{r_r[j, k]}{\sqrt{r_r^2}} \quad (4)$$

r_r being a random number from a continuous uniform distribution between -0.5 and 0.5 , $\bar{\cdot}$ being for this special case a spatial average and j, k ranging the indices of the cell of the injection plan (*i.e.* $j \in [0, 60]$ for the wall normal direction and $k \in [0, k_{max}]$ in the azimuthal direction). As the time step used in the computation is far less than the convection time through one cell in the streamwise direction, the spatial scheme would be unable to transport a white noise that is updated every iteration. To address this issue, it was chosen not to update the noise every iteration, but to keep it constant for 15 iterations between each update. This ensures that the scheme can discretize the noise while the spectral content is still rich enough in the high frequencies for the present study, a power spectral density of pressure perturbations created by the noise is presented in figure 2.

Appendix 2 : Azimuthal decomposition of the Jacobian operator

Since the solver FAST works internally with Cartesian coordinates, one has to first carry out a transformation to cylindrical coordinates to retrieve the axisymmetry of the flow using the following relation

$$\begin{pmatrix} \rho \\ \rho u_x \\ \rho u_r \\ \rho u_\theta \\ \rho E \end{pmatrix} = \begin{bmatrix} 1 & 0 & 0 & 0 & 0 \\ 0 & 1 & 0 & 0 & 0 \\ 0 & 0 & \cos(\theta) & \sin(\theta) & 0 \\ 0 & 0 & -\sin(\theta) & \cos(\theta) & 0 \\ 0 & 0 & 0 & 0 & 1 \end{bmatrix} \begin{pmatrix} \rho \\ \rho u_x \\ \rho u_y \\ \rho u_z \\ \rho E \end{pmatrix} \quad (5)$$

Under appropriate indexing of the degrees of freedom, the Jacobian operator can then be rearranged into the block-circulant form

$$\mathbf{J} = \begin{bmatrix} \mathbf{A}_0 & \mathbf{A}_1 & \dots & \mathbf{A}_{n-2} & \mathbf{A}_{n-1} \\ \mathbf{A}_{n-1} & \mathbf{A}_0 & \dots & \mathbf{A}_{n-3} & \mathbf{A}_{n-2} \\ \mathbf{A}_{n-2} & \mathbf{A}_{n-1} & \dots & \mathbf{A}_{n-4} & \mathbf{A}_{n-3} \\ \vdots & \vdots & \vdots & \vdots & \vdots \\ \mathbf{A}_1 & \mathbf{A}_2 & \dots & \mathbf{A}_{n-1} & \mathbf{A}_0 \end{bmatrix}, \quad (6)$$

where each line of blocks corresponds to a given azimuthal slice of the mesh and the block matrices $\mathbf{A}_0, \dots, \mathbf{A}_{n-1}$ have a size corresponding to such a slice (the size of a 2D problem). The block-circulant nature of the matrix comes from the numerical and physical equivalence of all azimuthal slices of the mean flow, which cannot be distinguished from one another. As shown by Schmid *et al.* [40], this block circulant matrix can then be transformed into a block-diagonal matrix

$$\tilde{\mathbf{J}} = \begin{bmatrix} \tilde{\mathbf{A}}_0 & & & & \\ & \tilde{\mathbf{A}}_1 & & & \\ & & \ddots & & \\ & & & & \tilde{\mathbf{A}}_{n-1} \end{bmatrix}, \quad (7)$$

with

$$\tilde{\mathbf{A}}_m = \mathbf{A}_0 + \rho_m \mathbf{A}_1 + \rho_m^2 \mathbf{A}_2 + \dots + \rho_m^{n-1} \mathbf{A}_{n-1}, \quad (8)$$

and $\rho_m = e^{\frac{j2\pi m}{n}}$ corresponding to a m -root of unity.

This leads to independent studies for each wavenumber of interest through the study of the eigenvalues of the reduced operator $\tilde{\mathbf{A}}_m$ instead of the full operator \mathbf{J} .

Appendix 3 : Numerical procedure for the Proper Orthogonal Decomposition

First, $N_r = 600$ snapshots are randomly sampled from the pool of filtered snapshots, then a Discrete Fourier Transform (DFT) is applied in the azimuthal direction, giving Fourier mode vectors $\hat{\mathbf{S}}^k(m)$, where k is the realisation number and m the azimuthal wavenumber of the mode. Due to the spectral transformation in the azimuthal direction, the vectors $\hat{\mathbf{S}}^k(m)$ correspond to bi-dimensional fields: they contain complex values associated with each flow variables at each pair (x, r) from the mesh. For a given wavenumber (m) of interest, the Fourier modes of all realisations are then stacked in a matrix $\hat{\mathbf{X}}_m$, which reads

$$\hat{\mathbf{X}}_m = \left[\hat{\mathbf{S}}^0(m), \hat{\mathbf{S}}^1(m), \dots, \hat{\mathbf{S}}^{N_r-1}(m) \right]. \quad (9)$$

This matrix is then processed similarly to a snapshot matrix in a classical POD decomposition: the i -th POD mode $\phi_i^{(m)}$ can be computed from the i -th left singular vector of $\hat{\mathbf{X}}_m$, which may be computed by solving the eigenproblem associated with the cross spectral density matrix

$$\hat{\mathbf{X}}_m \hat{\mathbf{X}}_m^* \mathbf{Q}_e \psi_i^{(m)} = \lambda_i \psi_i^{(m)}, \quad (10)$$

with \mathbf{Q}_e the inner product associated with the energy norm defined by Chu [50] :

$$\mathbf{Q}_e = \Omega \begin{bmatrix} \frac{|\bar{\mathbf{u}}|^2 + R\bar{T}}{\bar{\rho}} + a_1 a_2^2 & \frac{-\bar{u}_x(1+a_1 a_2)}{\bar{\rho}} & \frac{-\bar{u}_r(1+a_1 a_2)}{\bar{\rho}} & \frac{-\bar{u}_\theta(1+a_1 a_2)}{\bar{\rho}} & \frac{a_1 a_2}{\bar{\rho}} \\ \frac{-\bar{u}_x(1+a_1 a_2)}{\bar{\rho}} & \frac{\rho + u_x^2 a_1}{\rho^2} & \frac{\bar{u}_x \bar{u}_r a_1}{\rho^2} & \frac{\bar{u}_x \bar{u}_\theta a_1}{\rho^2} & \frac{-\bar{u}_x a_1}{\rho^2} \\ \frac{-\bar{u}_r(1+a_1 a_2)}{\bar{\rho}} & \frac{\bar{u}_x \bar{u}_r a_1}{\rho^2} & \frac{\rho + u_r^2 a_1}{\rho^2} & \frac{\bar{u}_r \bar{u}_\theta a_1}{\rho^2} & \frac{-\bar{u}_r a_1}{\rho^2} \\ \frac{-\bar{u}_\theta(1+a_1 a_2)}{\bar{\rho}} & \frac{\bar{u}_x \bar{u}_\theta a_1}{\rho^2} & \frac{\bar{u}_r \bar{u}_\theta a_1}{\rho^2} & \frac{\rho + u_\theta^2 a_1}{\rho^2} & \frac{-\bar{u}_\theta a_1}{\rho^2} \\ \frac{a_1 a_2}{\bar{\rho}} & \frac{-\bar{u}_x a_1}{\rho^2} & \frac{-\bar{u}_r a_1}{\rho^2} & \frac{-\bar{u}_\theta a_1}{\rho^2} & \frac{a_1}{\rho^2} \end{bmatrix} \quad (11)$$

$$a_1 = \frac{\bar{\rho}}{C_v \bar{T}} \quad (12)$$

$$a_2 = \frac{\frac{|\bar{\mathbf{u}}|^2}{2} - \bar{e}}{\bar{\rho}} \quad (13)$$

With Ω the local cell volume and e the internal energy. This norm is commonly used in order to describe fluctuation energy in compressible flow [51–53] and is more adapted than a simple kinetic energy norm often used for (quasi-)incompressible flows. The POD modes are ordered with respect to their contribution to the global dynamics, *i.e.* $\lambda_0 > \lambda_1 > \lambda_2 > \dots$, and for a given wavenumber (m), the relative contribution of the i -th POD mode is measured by the ratio $r_i = \lambda_i / \sum_k \lambda_k$.

In practice, the eigenmodes are computed by using the snapshots method of [54] which is a less costly but equivalent decomposition based on $\hat{\mathbf{X}}_m^* \mathbf{Q}_e \hat{\mathbf{X}}_m$ rather than (10). This provides the right singular vectors of $\hat{\mathbf{X}}_m$, from which one can easily retrieve the POD modes (see for instance [32] for details). Note that it is possible to localise the POD analysis to a given region of the flow by setting all coefficients of \mathbf{Q}_e associated with cells outside of this region to zero. The eigenvalue is then defined as the energy restrained to this specific zone.